Title
Controlling the Magnetic State of Nickel Nanocrystal in Granular Multiferroic Composites

Author
Sasaki, Stephen Shinjiro

Publication Date
2018

Peer reviewed|Thesis/dissertation

UNIVERSITY OF CALIFORNIA

Los Angeles

Controlling the Magnetic State of Nickel Nanocrystal in Granular Multiferroic Composites

A dissertation submitted in partial satisfaction of the requirements for the degree Doctor of Philosophy in Chemistry

by

Stephen Shinjiro Sasaki

2018

ABSTRACT OF THE DISSERTATION

Controlling the Magnetic State of Nickel Nanocrystal Arrays in Granular Multiferroic Composites

by

Stephen Shinjiro Sasaki

Doctor of Philosophy in Chemistry

University of California, Los Angeles, 2018

Professor Sarah H. Tolbert, Chair

Multiferroics are a broad class of materials, which couple multiple ferroic ordering parameters into a single composite—e.g., coupling ferroelectric and ferromagnetic materials. The key feature of multiferroic composites is the ability to control the magnetic (dipole) moments of the composite via an applied electric (magnetic) field. Depending on the coupling mechanisms between the two ferroic materials and the choice of materials, the properties of the multiferroic composite can differ wildly—permitting widespread applications such as field sensors, power

convertors, energy storing systems, cooling devices, memory systems, etc. Adding to the plethora of multiferroics, we will be focusing on granular multiferroics (GMF), which substitutes the ferromagnetic material with ferromagnetic nanocrystals, referred to as grains

Although only the size of the ferromagnetic material is being changed, GMF composites present new experiments and insights in controlling magnetism at the nanoscale. We use solution processed methods to synthesize superparamagnetic Ni nanocrystals for all of our GMF composites. We developed fabrication methods for strain-mediated GMF composites by employing the reactive Ni nanocrystal surface to bond to a PMN-PT piezoelectric substrate. The magnetic anisotropy of the strain-mediated GMF composite was shown to be controllable and reversible by applying an electric field induced piezoelectric strain. Because the PMN-PT cut used has a biaxial strain, compressive and tensile, we were able to observe inverse magnetic trends for the blocking temperature of the nanocrystal along the two strain axes. Other fabrication methods we developed, modified the nanocrystal surface with diacid ligands to study magnetic interparticle interactions, known as exchange coupling. Theoretical models of exchange coupled GMF composites predicted a novel magnetoelastic coupling mechanisms that can control the magnetic anisotropy of the ensemble by tuning the dielectric environment of the nanocrystal composite. Experimental work was carried out to fabricate and validate this exchange coupled GMF composite, making it the first demonstration of its kind. This thesis outlines our contributions to the ever-growing field of GMF by establishing methods for fabricating novel granular multiferroic composites and evaluating their unique coupling mechanism and magnetic properties.

The dissertation of Stephen Shinjiro Sasaki is approved.

Gregory P. Carman

Xiangfan Duan

Sarah H. Tolbert, Committee Chair

University of California, Los Angeles

2018

This manuscript is dedicated to Yung Kuo,

for five years of happy memories

We began our PhD journey as significant others and finished our PhD journey as

husband and wife

TABLE OF CONTENTS

LIST OF FIGURES VIII

ACKNOWLEDGEMENTS XIV

VITA XIX

CHAPTER 1. INTRODUCTION 1

CHAPTER 2. DEVELOPMENT OF A SIMPLE ADHESION METHOD FOR APPLICATIONS IN STRAIN-MEDIATED MAGNETOELECTRIC NANOCRYSTALS SYSTEMS 4

2.1 INTRODUCTION 4

2.2 EXPERIMENTAL METHODS 5

2.2.1 SYNTHESIS OF NI NANOCRYSTALS. 5

2.2.2 OXIDATION ADHESION PROCESS 6

2.2.3 CONTROLLED OXIDATION OF NANOCRYSTALS 7

2.2.4 SUBSTRATE PREPARATION 7

2.2.5. INSTRUMENTATION. 7

2.3. RESULTS AND DISCUSSION 7

2.4. CONCLUSION 15

CHAPTER 3. ANISOTROPIC ELECTRIC FIELD CONTROL OF MAGNETIZATION IN A STRAIN-MEDIATED, NANOCRYSTAL-BASED MULTIFERROIC COMPOSITE 15

3.1. INTRODUCTION 15

3.2. EXPERIMENTAL 17

3.2.1. NI NANOCRYSTAL SYNTHESIS. 17

3.2.2. PMN-PT. 19

3.2.3. FABRICATION OF THE GMF COMPOSITE. 19

3.2.4. MEASUREMENT 20

3.2.5. MODELING.....20

3.3. RESULTS AND DISCUSSION 23

3.3.1. MATERIALS CHARACTERIZATION. 23

3.3.2 VOLTAGE DEPENDENT MAGNETIC RESPONSE.....27

3.4. CONCLUSIONS 37

CHAPTER 4. TUNING EXCHANGE COUPLING IN A NEW FAMILY OF NANOCRYSTAL-BASED GRANULAR MULTIFERROICS USING AN APPLIED ELECTRIC FIELD.....38

4.1. INTRODUCTION TO GRANULAR MULTIFERROIC COMPOSITES 38

4.2. RESULTS AND DISCUSSION.....43

4.2.1. MATERIALS CHARACTERIZATION. 43

4.3.2. TEMPERATURE DEPENDENT MAGNETIC STUDIES. 44

4.3.3. ELECTRIC FIELD DEPENDENT MAGNETIC PROPERTIES.....49

4.4. CONCLUSION 53

4.5. METHODS 54

4.5.1 SYNTHESIS OF NI NANOCRYSTALS. 54

4.5.2. FERROELECTRIC MATERIALS. 55

4.5.3. CONTROLLING NANOCRYSTAL INTER-PARTICLE DISTANCES.....56

4.5.4. GRANULAR MULTIFERROIC COMPOSITE. 57

4.5.5. MAGNETIC AND ELECTRICAL MEASUREMENTS. 58

4.5.6. MODELING OF GMF COMPOSITES. 58

APPENDIX 59

BIBLIOGRAPHY: 70

LIST OF FIGURES

Figure 2.1. X-ray photoelectron spectroscopy (XPS) spectra of silicon substrates in the Si 2p range, titanium substrates in the Ti 2p range, nickel nanocrystals in the Ni 2p range: (a) Si substrate, (b) SiO_2 substrate, (c) Ti substrate, (c) TiO_2 substrate, (d) Ni nanocrystals, (e) NiO nanocrystals.

Figure 2.2. Scanning electron microscope (SEM) images varying substrate reactivity (columns) and nanocrystal reactivity (rows). (a) Images before scotch tape removal. (b) Images after scotch tape removal.

Figure 2.3. Room temperature magnetic hysteresis loops from SQuID magnetometry. Partial loop shown for clarity. (a) Strong adhesion of Ni nanocrystals on Ti substrate. (b) Weak adhesion of Ni nanocrystals on SiO_2 substrate. (c) No adhesion of NiO nanocrystals on SiO_2 substrate. Right graph shows coercivity trend of the three samples.

Figure 2.4. Magnetic hysteresis loops of (a) Unadhered NiO nanocrystals before plasma etching and (b) adhered NiO after reduction to Ni using reducing plasma.

Figure 2.5. Zero field cooled magnetization curves of nanocrystals not adhered (black) and adhered (blue) with blocking temperatures of 75 K and 100K, respectively. Shoulder on blue curve from the presence of non-adhered nanocrystals. Normalized average magnetic moment (a.u.) versus applied field (Oe) of adhered samples show no exchange coupling present, see inset.

Figure 3.1. Representative powder XRD of the Ni nanocrystals used for this work. The data confirms that samples have the correct crystals phase and the diffraction shows no evidence of significant oxidation. The inset shows an SEM shows a uniform monolayer of monodispersed 14 nm Ni nanocrystals.

Figure 3.2. Normalized out-of-plane M-H loops for nanocrystals with no adhesion (surface oxidized in solution and then spin coated monolayer on SiO_2 wafer, red lines), and nanocrystals that are covalently bonded to the substrate (chemically oxidized onto a PMN-PT/Ti/TiO_x wafer, blue lines), collected at both 298K and 100K. Data collected at lower T shows increased coercivity, but the difference between the two samples remains constant.

Figure 3.3 Strain response of PMN-PT as a function of electric field. The (100) axis develops a compressive strain, while the (011-) axis develops a tensile strain. Cartoon schematics of Ni nanocrystals adhered to the Ti/PMN-PT substrate. Unstrained the nanocrystals are magnetically isotropic, however under strain, the magnetic moments develop an easy and hard-axis, corresponding to the (100) and (011-), axes respectively.

Figure 3.4. Normalized ZFC curves as a function of applied voltage, where compression in the (100) axis, shifts T_b to higher T, and tension in the (011-) axis, shifts T_b to lower T. The insets show the data on an expanded y-scale to make the shifts easier to see. The shifts in T_b with voltage go in opposite directions due to the anisotropic strain. Cycled 0 V data show that changes are reversible and the strain can be released after the applied bias is removed.

Figure 3.5. Normalized ZFC curve as a function of applied voltage for the (011-) axis. The applied voltage leads to tension in the (011-) axis, which shifts T_b to lower T. The inset again show

the data on an expanded y-scale to make the shifts easier to see. The higher initial blocking temperature for this sample allows for larger shifts and thus better characterization of the ability for an applied voltage to reduce the hard-axis T_b.

Figure 3.6. Monte Carlo simulation of the strain-mediated GMF composite. From the initial (pre-strained) state an induced tension and compression produces the observed experimental trends.

Figure 3.7. The relative magnetization change as a function of voltage shows increasing magnetization along the (011-) hard-axis, and decreasing magnetization along the (100) easy-axis. When the applied bias returns to 0 V, the magnetization mostly returns to its original state, although some residual strain is observed in the (100) easy-axis direction.

Figure 3.8. Monte-Carlo simulation of ZFC curves measured along the (011-) axis, with different initial magnetic states. Blue curve, represents a system starting with magnetic moments aligned along the (100) axis, i.e. a strained system. Red curve, represents a system starting with magnetic moments randomized, i.e. an unbiased system. The modeled system suggests the initial magnetic orientation prior to heating and measurement influences the relative change in magnetization observed experimental. Lines are provided as guides for the eyes.

Figure 3.9. (a) ZFC measurements along the (100) easy-axis for a system cooled without an applied electric field. The data show a voltage dependent shift in the hard-axis T_b (see inset for normalized data with an expanded y-scale), but the change in magnetization with voltage is very small and shows no trend with bias strength. (b) Comparison of the relative change in peak magnetization for systems cooled with and without an applied electric field.

When cooled with an electric field the hard and easy axes show divergent changes in magnetization intensity with an applied bias, while when cooled without an electric field there is essential no change.

Figure 4.1. Cartoon showing the influence of the dielectric constant of a ferroelectric matrix, FE, on inter-particle exchange interactions (J) in GMF composites. The upper panel shows two interacting magnetic grains with magnetic moments $M_{1,2}$. Interaction occurs via virtual hopping of electrons (e) between grains with probability t. In a nanocrystal system, electron hopping is due to the Coulomb blockade effect, creating a gap, E_c. The exchange coupling can be roughly described as $J \sim t^2/E_c$. The Coulomb gap strongly depends on the dielectric constant of the surrounding media due to screening of image charges. When the dielectric constant is low (left panel) the gap is large and hopping (exchange) is suppressed, resulting in a disordered (superparamagnetic) magnetic state with no long-range order (bottom left). In contrast, strong exchange coupling occurs when the dielectric constant is high (right panel) resulting in an ordered (ferromagnetic) state with long-range ordering (bottom right).

Figure 4.2: (a) TEM images of the monodispersed nickel nanocrystals used in this work. (b) Powder XRD of the Ni nanocrystals confirms that they have the correct crystal structure (red stick pattern) and that no crystalline NiO is present in the sample (black stick pattern). (c) The color change observed in our TTF-CA indicates a phase transition from the paraelectric phase at room temperature to the ferroelectric phase at liquid nitrogen temperatures. TTF-CA has an expected 81 K T_C and a 10-fold increase in dielectric

constant near the transition. (d) Powder XRD of TTF-CA. Peak positions are in good agreement with literature values.

Figure 4.3: Top panel: SQuID magnetometry measurements of coercivity as a function of temperature. The data shows increasing coercivity with decreasing inter-particle distances due to increasing dipole-dipole and exchange couplings. Markers represent experimental data; solid lines are guides for the eyes. (a) nanoparticles in paraffin wax (black); (b) nanoparticles linked by glutaric acid (red); (c) nanoparticles linked by oxalic acid (green); and (d) aggregated, ligand stripped (blue). Bottom panel: SQuID magnetometry measurements of coercivity as a function of temperature for, (a) uncoupled wax dispersed nanocrystals (red); (b) exchange coupled oxalic acid linked nanocrystals (green); and (c) exchange coupled nanocrystals in a TTF-CA matrix, forming a GMF composite (blue). Markers indicate experimental data. Solid lines are derived from Monte-Carlo simulations of the experimental data.

Figure 4.4. Electric field dependence for two different GMF composites. In both cases, the markers represent experimental data and the solid lines represent theoretical models. (a) Coercivity as a function of applied voltage is plotted for a TTF-CA GMF composite, with data obtained at 65 K and 80 K. The inset shows a cartoon schematic of the parallel plate capacitor setup used for biasing. At both temperatures, coercivity can be modified with a voltage and in both cases we observe, first an increase in the coercivity followed by a decrease, which is likely caused in part by ferroelectric domain reorientation. For the 80 K sample near the T_C of the TTF-CA, the magnitude of the change in coercivity is much larger, suggesting that the dielectric changes are enhanced by contributions from the paraelectric to ferroelectric phase transition. (b) Coercivity across the full temperature

range for a KDP GMF composite at 0 V, 100 V, and 200 V. The inset shows a cartoon schematic of the parallel plate capacitor setup used for biasing the KDP GMF composite. Again, we observe that the coercivity first increases, when a moderate voltage of 100V is applied to the sample, and then decreases somewhat, when a larger voltage is applied. KDP should not have any phase transitions in this temperature range, so these changes are likely to be a purely domain alignment effect.

Appendix figure A1: Cartoon schematic and microscopy images of diacid linked Ni nanocrystals. (a) 0 carbon, aggregated nanocrystals without diacid linkers. (Inset) SEM of aggregated nanocrystals (b) 2 carbon, oxalic acid linked Ni nanocrystals. (c) 5 carbon, glutaric acid linked Ni nanocrystals.

Appendix figure A2: M-H curves across a range of temperatures for ligand stripped nanocrystal sample used in the top panel figure 3. Shape markers represent experimental data and solid lines are provided as a guide for the eyes. Inset provides the full range of the applied magnetic field. Increasing coercivity is observed as a function of decreasing temperature.

ACKNOWLEDGEMENTS

I would like to thank all of the people who made this journey possible. My passion for science began when I was very young, and has luckily been nurtured over the years by so many people. I especially want to thank my mother and step-father for always supporting my relentless inquisitiveness. My mother especially seemed to never doubt my potential in anything I pursued, for better or worse. I would also like to thank my father and step-mother who certainly helped emphasized the practical aspects of life— this served me well. Most of all, I am deeply grateful to my loving wife who was always there for me, whether it was mentoring me through quantum mechanics or supporting me through many a sleepless night in the lab or being a role model for never giving up. Because of her, my wife, we have not only survived our individual Ph.D. programs, but we have also spent five of the happiest years of our lives together.

I would like to thank all the wonderful faculty who had the privilege to work with and learn from. I was incredibly fortunate to have Professor Sarah Tolbert as my advisor. Professor Tolbert was, from the very first day I met her and to this day, a deeply caring individual, who is not only passionate about science, but also passionate about life. I was also privileged to receive guidance from Professor Greg Carman and Professor Jane Chang as part of the Center for the Translational Applications of Nanoscale Multiferroic Devices (TANMS). My experience with the leadership team in TANMS provided me the skill set for leadership roles and this was an invaluable and unexpected benefit of my PhD education. Finally, I would like to thank Professor Igor Beloborodov for engaging with me in many informative discussions over the years, and contributing important theoretical insights to my research.

I would also like to thank my colleagues in TANMS as well as the entire administrative team. As Professor Carman would frequently say, “TANMS is a family” and he was absolutely right. I would like to especially thank the TANMS Student Leadership Council for persevering through all my many ups and downs. I want to especially thank Kevin Fitzell for being a dependable colleague, a friend through SLC duties, research collaborations, outreach and education, and so much more. There are honestly too many TANMS members that I would like to thank to mention them all here, so to all the TANMS researchers who spent countless hours working with me on various projects, I thank you all for making my PhD the wonderful experience it was. I would like to specifically mention the TANMS administrative team who helped me navigate all things TANMS; Tsai-Tsai O-Lee and Michelle Schwartz for always helping me fix my mistakes, and Maria del Pilar O'Cadiz for always helping me to cause trouble!

I want to thank all of the collaborators who helped make my research possible. I cannot thank Oleg Udalov enough for his incredible theoretical models which guided so much of my experimental work on granular multiferroic composites. Without question, my PhD would be entirely different without his theoretical work. I would also like to thank Xiang Li for helping me with sputtering of various materials over the years. I would also like to thank Andres Chavez, Kevin Fitzell, Mohanchandra Panduranga, and Colin Rementer for helping me in my research with strain-mediated granular multiferroics. I would especially like to thank all of the TANMS SQuID users for sharing their unused time with me! In total, I estimated at least 3000 hours spent with the SQuID magnetometer; I could not have finished my work without those hours donated.

I would like to thank Shauna Robbennolt who was one of the most influential people in my PhD studies. I thank her for her endless help in educating me about magnetism and for always

finding time to help me. I would also like to thank the Tolbert Lab Magnetics Team (Abraham Buditama, Ty Karaba, Jeff Kurish, and Shreya Patel) for making magnets the best research field to be in. I would also like to thank the Tolbert Group as a whole for so many excellent memories. I wish to particularly thank Ben Lesel for 10 years of uniquely memorable times together, and Yan Yan for 5 years of much needed "normal" friendship! I would also like to thank Terri Lin for all the experience that jump started my career in EH&S. After many trying times, I came to respect and admire her as an incredibly dedicated and hardworking researcher, and I have benefitted much from our initial safety conflicts. Last but not least, I would like to thank my undergraduate mentees, Eduardo Garcia and Momoko Ishii, for always showing so much dedication and curiosity, and helping me to grow as a mentor.

Finally, I would like to thank many members of the Chemistry and Biochemistry Department. I had the privilege to the be the teaching assistant for Dr. Henary for every quarter of my PhD, except one. He is an inspiring educator and an excellent mentor to both his teaching assistants and his students. I would also like to thank Maria-Kris Dimaano-Slanga and Erika De Guzman for always putting up with me in Lab Support. I would also like to thank Dr. Janette Kropat for always helping me fix the lab or report a problem. Lastly, I would like to thank Dr. Igancio Martini who ran the Molecular Instrumentation Center and was always there to provide insight and guidance with his unique sense of humor.

My work here was supported by the NSF Nanosystems Engineering Research Center for Translational Applications of Nanoscale Multiferroic Systems (TANMS) under Cooperative Agreement Award EEC-1160504.

Previous Publications and Contributions of Co-authors

Chapter 2 is a version of Stephen S. Sasaki, Shauna Robbennolt, Eduardo Garcia, Sarah H. Tolbert, "Development of a simple adhesion method for applications in strain-mediated magnetoelectric nanocrystals systems." Eduardo Garcia did most of the solution processed synthesis of Ni nanocrystals for this work. I did the remaining fabrication and characterization of the composites as well as the manuscript writing. Shauna Robbennolt provided significant guidance and helped troubleshoot the project during its early stages. Sarah Tolbert provided guidance throughout the project and edited the manuscript as well as will help to submit the manuscript for publication soon after this dissertation is filled.

Chapter 3 is a version of Stephen S. Sasaki, Oleg G. Udalov, Andres Chavez, Kevin Fitzell, Igor Beloborodov, Sarah H. Tolbert, "Voltage controlled magnetic anisotropy in a strain-mediated granular multiferroic system of Ni/Ti/PMN-PT." Oleg Udalov provided all of the modeling and theoretical simulations presented in this work, as well as contributed to manuscript writing. Andres Chavez provided experimental data on the PMN-PT substrates used for this work, as well as contributed to manuscript writing. Kevin Fitzell assisted with in-situ SQuID magnetometry measurement, as well as characterization. I did the remaining experimental work and characterization presented in this work, as well as the manuscript writing. Sarah Tolbert and Igor Beloborodov provided guidance throughout the project and edited the manuscript as well as will help to submit the manuscript for publication soon after this dissertation is filled.

Chapter 4 is a version of Stephen S. Sasaki, Oleg G. Udalov, Momoko Ishii, Shaunna Robbennolt, Kevin Fitzell, Igor Beloborodov, Sarah H. Tolbert, "Tuning the exchange coupling in granular multiferroics with electric field" Oleg Udalov provided all of the modeling and theoretical simulations presented in this work, as well as contributed to manuscript writing. Momoko Ishii

contributed the majority of synthesis of Ni nanocrystals and the experimental results of using diacids, as well as contributed to the sample characterization for this data. Kevin Fitzell assisted with in-situ SQuID magnetometry measurement, as well as characterization. I did the remaining experimental work and characterization presented in this work, as well as the manuscript writing. Sarah Tolbert and Igor Beloborodov provided guidance throughout the project and edited the manuscript as well as will help to submit the manuscript for publication soon after this dissertation is filled.

VITA

Education

B.S. Chemistry, University of California, Irvine 2008 – 2013

Research Experience

University of California, Los Angeles, *Tolbert, Graduate Researcher,* Sept, 2013 – Oct, 2018

University of California, Irvine, *Apkarian, Undergraduate Researcher,* 2009 – 2013

Publication

- S. Robbennolt, **S. S. Sasaki**, T. Wallace, M. Bartholomew, S. H. Tolbert. **Adv. Mater. Lett**., 2018, 9 (5), pp 345-352. Fabrication and Magnetic Properties Of Sol-Gel Derived NiZn Ferrite Thin Films For Microwave Applications.
- M., Xin, G.Yu, S. A. Razavi, **S. S. Sasaki**, X. Li, K. Hao, S. H. Tolbert, K. L. Wang, and X. Li. *Phys. Rev. Lett. 119, 027202 (2017), arXiv preprint arXiv:1706.00535.* Dzyaloshinskii Moriya interaction across antiferromagnet/ferromagnet interface.
- **Sasaki, S. S.**, Zhang, Y. N., Dey, S., Tallarida, N., El-Khoury, P. Z., Apkarian, V. A., & Wu, R. *The Journal of Physical Chemistry C, 118(50), 29287-29293 (2014).* Intrinsically Conductive Organo–Silver Linear Chain Polymers $[-S–Ag–S–Biphenyl-]_n$ Assembled on Roughened Elemental Silver.
- **Sasaki, S. S.**, Perdue, S. M., Perez, A, R., Tallarida, N., Majors, J, H., and Apkarian, V. Ara, Lee, Joonhee. *Review of Scientific Instruments, 84, 096109 (2013).* Automated Electrochemical Etching and Polishing of Silver Scanning Tunneling Microscope Tips.

Presentations

- **62nd Annual Conference on Magnetism and Magnetic Materials,** Pittsburgh, PA. Oral Presentation. *Nov. 07, 2017* **S. S. Sasaki**, Shauna Robbennolt, Xiang Li, Kang Wang, Pedram Khalili, Sarah H. Tolbert. *Multiferroic and Magnetoelectric Control of Magnetism in Nanocrystal Arrays.*
- **62nd Annual Conference on Magnetism and Magnetic Materials,** Pittsburgh, PA. Oral Presentation. *Nov. 10, 2017.* **S. S. Sasaki**, Oleg Udalov, Shauna Robbennolt, Momoko Ishii, Igor Beloborodov, Sarah H. Tolbert. *Experimental Demonstration of A Novel Type of Magnetoelectric Coupling Based on Interparticle-Exchange Interactions.*
- **International Conference on Advances in Functional Materials**, Los Angeles, CA. Poster Presentation. *Aug 05, 2017* **S. S. Sasaki**, O. G. Udalov, S. Robbennolt, I. S. Beloborodov, S. H. Tolbert. *Development of A New Type of Magnetoelectric Coupling.*
- **TANMS Year 5 NSF Annual Review Site Visit**, Los Angeles, CA. Poster Presentation. *May 02, 2017.* **S. S. Sasaki**, O. G. Udalov, S. Robbennolt, I. S. Beloborodov, S. H. Tolbert. *Interparticle-exchange coupling in granular multiferroic composites.*
- **TANMS Year 4 NSF Annual Review Site Visit**, Los Angeles, CA. Poster Presentation. *May 17, 2016.* **S. S. Sasaki**, S. Robbennolt, L. T. Schelhas, S. H. Tolbert. *Development of Nanocrystal-Based Magnetoelectric Composites.*
- **TANMS Year 3 NSF Renewal Review Site Visit**, Los Angeles, CA. Poster Presentation. *Apr 30, 2015.* **S. S. Sasaki**, L. T. Schelhas, M. Nowakowski, S. Robbennolt, T. Karaba. *Magnetoelectric Control of Magnetic State in Ni and FeRh Nanocrystals*

CHAPTER 1. INTRODUCTION

The well-studied properties of bulk materials can be tremendously different from their nanoscale counterparts. Among the top materials most influenced by changes in scale would be magnetic materials. This is because the behavior of magnetic moments is a collective phenomenon, having both long and short-range interactions which depend greatly on the spatial configuration of the magnetic moments. For instance, changes in a magnetic nanocrystal's size, shape, and crystal structure all influence the short-range interactions within a magnetic material, but one must also consider long-range and external interactions such as, interparticle interactions, interfacial interactions, and environmental influences. The work presented here investigates this complex system of nanomagnets and explores how to control the magnetic state of nickel nanocrystals integrated into multiferroic composites. There is significant interest in controlling magnetism at the nanoscale, having clear benefits for future memory applications, but also multiferroics in general is a versatile class of materials in its own right. Multiferroic composites are capable of demonstrating coupling between both the magnetic and electric degrees of freedom. This physical effect, achieved by coupling a ferromagnetic and ferroelectric material, is quite important for numerous commercial applications — e.g. magnetic field sensors, power convertors, energy storing systems, and cooling devices. The work presented here focuses on two different multiferroic systems: strain-mediated granular multiferroics and exchange-coupled granular multiferroics. Both systems use nickel nanocrystals, or grains, as the ferromagnetic materials, with the former relying on strain coupling to a piezoelectric substrate and the later utilizing a novel mechanism of interparticle interactions, known as exchange coupling.

Chapter 2 and 3 are an investigation of strain-mediated granular multiferroic (GMF) composites. Chapter 2 is focused on the initial fabrication of the strain-mediated GMF composite. For strain-mediated GMF composites, the nanocrystals require a strong adhesion to the piezoelectric substrate in order to observe any magnetoelastic behavior. Here, we discuss the specific challenges of developing fabrication methods that can strongly adhere nanocrystals to a substrate, while also simultaneously being gentle enough to preserve the unique nanoscale magnetic properties. Our methods preserve the nanocrystal properties by avoiding any external fabrication methods, such as annealing or etching. Instead we employ a simple self-assembly method which utilizes the intrinsic high surface energy of the nanocrystals to form metal-oxide bonds as a form of adhesion. We show that our oxidation adhesion method produces an isotropic strain which can be observed as a magnetoelastic effect in super quantum interference device (SQuID) magnetometry measurements. Furthermore, we show that the oxidation adhesion process is reversible using reducing or oxidizing plasmas to control the state of adhesion.

Chapter 3 investigates the magnetoelectric characteristics of a strain-mediated GMF fabricated using the methods discussed in Chapter 2. With this system we are able to investigate strain-mediated means to control magnetic elements at the nanoscale. This is of particular interest to memory applications as a potential means to stabilize magnetic elements below the SPM limit. The strain-mediated GMF composite consists of single domain nickel nanocrystals adhered to a PMN-PT $[Pb(Mg_{1/3}Nb_{2/3})O_3]_{0.68}[PbTiO_3]_{0.32}$ substrate with a Ti interfacial layer. The PMN-PT used has an electric field induced biaxial strain response in-plane, which transfers to the adhered Ni nanocrystals. This biaxial strain introduces magnetic anisotropy into the nanocrystals by magnetoelastic effects. The added magnetic anisotropy forces the nanocrystals to develop easy and hard axes, which is observed by zero-field cooled (ZFC) measurements using a SQuID

magnetometer. Measurements along the easy axis show a deeper energy well as evidence by an increased blocking temperature with applied voltage. The hard axis shows an inverse behavior. The strain-mediated GMF composite is also shown to be reversible, showing its original magnetic characteristics when the applied electric field is removed.

In Chapter 4 we experimentally demonstrate for the first time, a new class of GMF composite based on interparticle interactions, known as exchange-coupling. Theoretical modeling of this GMF composite that predicted the ensemble spin orientation of closely spaced magnetic nanocrystals can be tuned by interparticle exchange interactions—which in turn can be controlled by modifying the dielectric environment of the nanocrystals. By tuning the extent of exchange coupling, the composite material can be switched between a superparamagnetic, or magnetically fluctuating, state and a ferromagnetic, or magnetically fixed, state. The composite consists of Ni nanocrystals integrated with a ferroelectric (FE) matrix, housed in a parallel plate capacitor setup. We demonstrated the dielectric environment of the FE matrix could be tuned by both thermal transitions and an applied electric field, which in turn controlled the magnetic properties of the GMF composite.

The work demonstrated here investigates GMF systems for their ability to control magnetism at the nanoscale. In general, we explored various fabrication methods that relied on controlling the nanoscale architecture of the systems via solution processed and self-assembly methods. With these composite materials, we were then able to observe new magnetic characteristics that stemmed from the unique magnetic couplings in our work.

CHAPTER 2. DEVELOPMENT OF A SIMPLE ADHESION METHOD FOR APPLICATIONS IN STRAIN-MEDIATED MAGNETOELECTRIC NANOCRYSTALS SYSTEMS

2.1 INTRODUCTION

Incorporation of colloidal magnetic nanocrystals could provide new avenues toward addressing various limitations in memory research, due to having exceptional nanometer scalability, unique tunable magnetic properties (size, shape, composition), and being synthetically cost effective. [1-7] Currently, research is progressing toward a universal memory, having non-volatile elements with a high bit density and low power consumption all on a single chip. [8-11] Among the most promising systems toward this goal, strain-mediated magnetoelectric composites have already demonstrated both non-volatile and low power consumption memory by employing piezoelectric strain to lower the magnetic anisotropy of magnetostrictive elements. [12-16] Integration of magnetostrictive nanocrystals with strain-mediated magnetoelectric composites could yield highly scalable bit densities of magnetic nanocrystal-elements below even the superparamagnetic limit, due to an enhanced magnetic stability gained from the strain anisotropy. [17, 18] This would be a promising step toward the development of universal memory. However, methods for producing efficient strain coupling of magnetostrictive nanocrystals to a strain medium must first be developed and thus is the focus of this work.

Integrating nanocrystals into strain-mediated composites, while simultaneously preserving the nanoscale properties, is particularly challenging due to the intrinsic size and organic capping ligands of colloidal nanocrystals. [2, 19-21] Standard methods to strain materials, such as epitaxial growth for thin-films or encasing particles in a strain medium, are ineffective for nanocrystals, due

to limited surface areas and the presence of organic capping ligands that allow for slip at the nanocrystal interface. [22, 23] Chemical methods for removing/exchanging the surface-capping agents tend to be material specific and often negatively impact the physical/material properties of the nanocrystals. [24-26] Direct methods, such as annealing nanocrystals to a strain medium can develop adhesion; however at the needed temperatures the high surface energy of the nanocrystals favors sintering into disordered islands/films. [27, 28]

In this work, a simple self-assembly method is presented that utilizes the intrinsic high surface reactivity of nickel nanocrystals to form strong metal-oxide bonds directly between the nanocrystals and various surfaces. X-ray photoelectron spectroscopy (XPS) investigations indicate the adhesion mechanism necessitates a high oxidation potential surface capable of metal-oxide bond formation. Methods to control the extent of adhesion are demonstrated by varying the oxidation potential of the nanocrystal and substrate surfaces. Superconducting quantum interference device (SQuID) magnetometry is used to characterize the adhered magnetic nanocrystals, which develop an interfacial stress resulting in a 40 Oe increase in coercivity and a 25 K shift in blocking temperature. Our results are a promising step toward developing nanocrystal-based strain-mediated magnetoelectric composites, with the potential to achieve ultra-high bit densities using strain coupled nanocrystals as magnetostrictive elements.

2.2 EXPERIMENTAL METHODS

2.2.1 Synthesis of Ni nanocrystals. Synthesis of nickel nanocrystals followed a modified version of Carenco, S. et al.[2929]. In general, nickel nanocrystals were synthesized by a thermal decomposition of 2 mmol nickel acetylacetonate in the presence of 14 mmol oleylamine (4.45 mL),

1 mmol oleic acid (0.315 mL), 1 mmol trioctylphosphosphine (0.446 mL), and sufficient 1-octadecene to fix the total volume at 7 mL. Under flowing argon, the solution was stirred at 70 ˚C for 20 minutes to dissolve precursors and further degassed at 130 ˚C for 30 minutes. The solution was then refluxed under an inert atmosphere at 220 ˚C for 45 minutes (ramp rate 15 ˚C/min) and then rapidly cooled to room temperature after completion.

The nanocrystal solution was purified three times using 1 mL hexanes and 40 mL of 190 proof ethanol. A 1" N52 neodymium magnet was used to quickly extract the nanocrystals (minutes), however standard centrifugation methods following the same time scale should work as well. Once the supernatant was clear, limited hexanes and 200 proof ethanol were used to remove excess water introduced during the original purification step. The final solution was suspended in 20 mL of hexanes and used immediately. Note that after the nanocrystals are exposed to water from the initial purification step, the solution must be used within several hours or the solution will precipitate, adhering to the container walls or aggregating in solution.

2.2.2 Oxidation adhesion process. In order to adhere the nanocrystals to various surfaces using the oxidation adhesion process, only freshly purified solutions of fully suspended nanocrystals were used. In general, substrates of various surfaces were submerged into the fresh nanocrystal solution and gently mixed for several minutes to an hour. A slight change in color of the substrate surface was noted due to the presence of a monolayer of nanocrystals physisorbed onto the substrate. The 5% water content used during the original purification of the nanocrystals (190 proof ethanol) was found to be key in initiating the self-assembly of nanocrystal onto the substrates. Without the 190-proof ethanol purification step, self-assembly would still occur, however substantially longer time is required to develop full monolayers. After the monolayers were developed, the substrate was transferred into a solution of pure hexanes and then sonicated

for 15 minutes. This washing was performed multiple times with fresh hexane solutions until clean. Once cleaned the substrates are allowed to dry in air. Nanocrystals on the substrate require several hours under ambient air conditions to become fully adhered.

2.2.3 Controlled oxidation of nanocrystals. As a control, Ni nanocrystals from the above solution were oxidized, yielding a NiO surface, by sonicating the solution with water and ethanol for several hours with mild heating (40 ˚C), until the nanocrystals favored the polar phase. The polar phase was then purified several times to remove any non-polar soluble nanocrystals.

2.2.4 Substrate preparation. Substrates of silicon, silicon dioxide, titanium, and titanium dioxide were prepared using various methods described below and then characterized via XPS. Si substrates were developed by etching as-purchased silicon wafers with hydrofluoric acid to remove any native oxide layer present. SiO_2 substrates were developed by 45 minutes of oxygen plasma of the as-purchased silicon wafers. [30] Ti substrates were produced through electron beam deposition of titanium (25 nm) on as-purchased silicon wafers and stored under inert atmosphere to limit oxidation. TiO_2 substrates were developed by 45 minutes of oxygen plasma of the Ti substrates prepared previously. [31]

2.2.5. Instrumentation. Magnetic measurements were conducted using a superconducting quantum interference device (SQuID) magnetometer (Quantum Design, MPMS XL-5). Oxidation potential of surfaces and samples carried out using X-ray Photoelectron Spectroscopy (XPS) from a Kratos Axis Ultra DLD spectrometer with a monochromatic Al (Kα) radiation source. Scanning electron microscope (SEM) images taken via JEOL JSM-6700F FE-SEM.

2.3. RESULTS AND DISCUSSION

The oxidation adhesion process developed to adhere nanocrystals to various substrates utilizes self-assembly and exploits the high surface reactivity of nanocrystals to develop strong metal-oxide bonds to the substrates through chemisorption. In order to understand this process, the surface oxidation of the nanocrystals and substrates were controlled to determine the effects on adhesion and investigated by XPS, SEM, and SQuID magnetometry.

The nanocrystals and substrates described in the experimental section above have been categorized as either unoxidized or oxidized and are referred to as Si or SiO_2 and Ti or TiO_2 for the substrates and Ni or NiO for the nanocrystals. XPS of the Si 2p spectra for Si and SiO_2 substrates are shown in figure 2.1a and 2.1b, respectively, with both substrates having expected Si^0 peaks at 99.4 eV and 100 eV. The peak at 103.5 eV assigned to Si^{4+} indicates oxidation characteristic of SiO_2, while the absence of this peak in Si substrate confirms pure Si. The Ti 2p XPS spectra for Ti and TiO_2 substrates are shown in figure 2.1c and 2.1d, respectively, with both spectra showing expected Ti^{4+} peaks at 458.6 eV and 464.7 eV, as well as Ti^0 peaks at 453.4 eV and 459.5 eV. For the TiO_2 substrate, the peak intensity ratio of Ti^{4+}/Ti^0 is much higher, suggesting greater oxidation extent compared to the Ti substrate. In addition, the absence of the Ti^{2+} peaks at 457 eV and 463.1 eV indicates further oxidation for the TiO_2 substrate. [31] The Ti substrate can be confirmed as predominately Ti, however it does show weak Ti^{2+} and Ti^{4+} peaks, which suggests partial oxidation of the as-deposited titanium is present due to the formation of a native oxide. The XPS spectra of Ni 2P for Ni and NiO nanocrystals are shown in figure 2.1e, f, composed of two sets of the spin-orbit doublet of Ni $2p_{3/2}$ and Ni $2p_{1/2}$. The peaks at 852.6 eV and 869.9 eV assign to Ni^0 and the peaks at 855.7 eV and 873.0 eV represent Ni^{2+}, as well as the presence of satellite features observed in

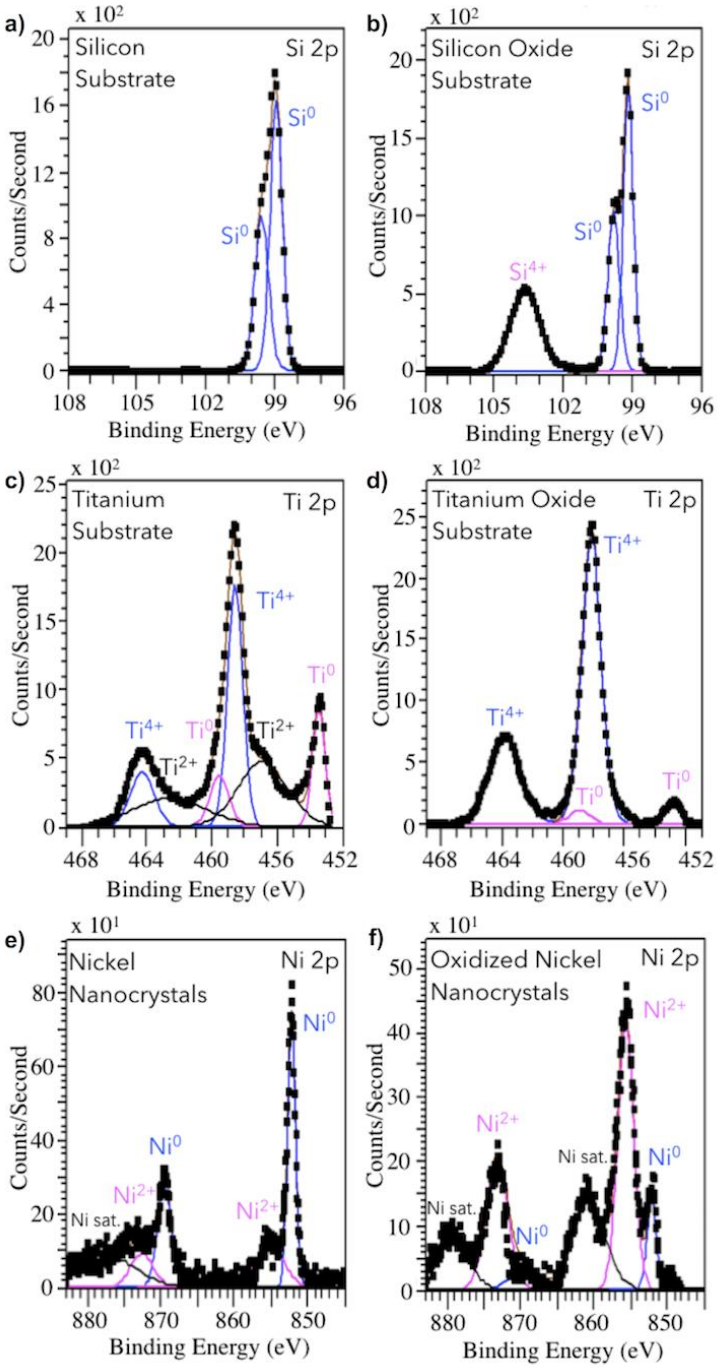

Figure 2.1. X-ray photoelectron spectroscopy (XPS) spectra of silicon substrates in the Si 2p range, titanium substrates in the Ti 2p range, nickel nanocrystals in the Ni 2p range: (a) Si substrate, (b) SiO_2 substrate, (c) Ti substrate, (c) TiO_2 substrate, (d) Ni nanocrystals, (e) NiO nanocrystals.

literature. [32] Due to the large difference in the peak intensity ratio of Ni^{2+}/Ni^{0}, between the Ni and NiO nanocrystals, it suggests significant oxidized content is present for the NiO nanocrystals compared to the as-synthesized Ni nanocrystals.

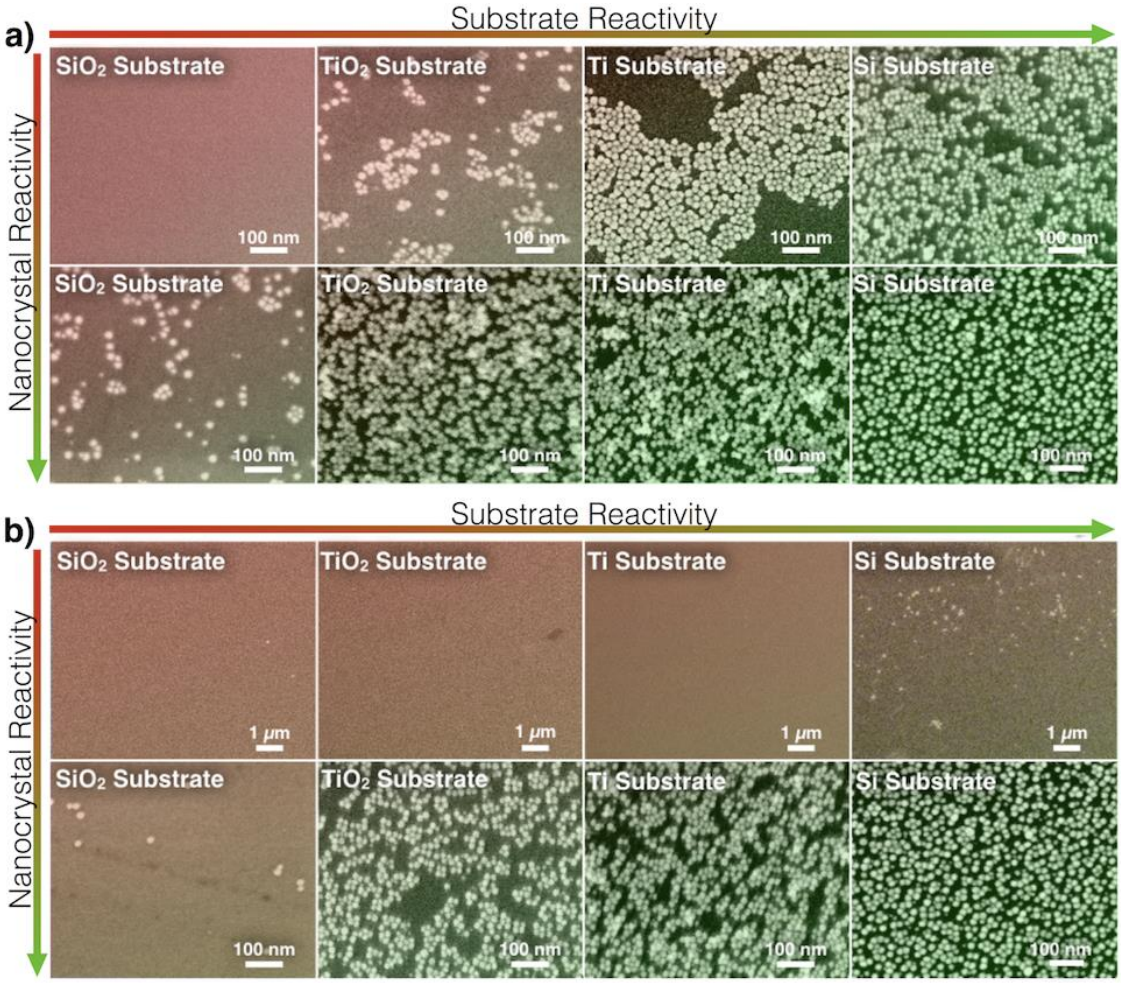

Figure 2.2. Scanning electron microscope (SEM) images varying substrate reactivity (columns) and nanocrystal reactivity (rows). (a) Images before scotch tape removal. (b) Images after scotch tape removal.

In order to generalize a mechanism of the oxidation adhesion process, the process was carried out with all combinations of nanocrystals and substrates characterized by XPS previously. SEM

images, varying substrate reactivity (columns) and nanocrystal reactivity (NiO & Ni nanocrystals top & bottom row, respectively) are shown in figure 2.2a, with adhesion of the nanocrystals seen to trend diagonally across the table. It is important to note that the nanocrystals in figure 2.2a are only physisorbed onto the substrate and can all be readily removed using scotch tape initially. However, after several hours in ambient air conditions the Ni nanocrystals adhered to TiO_2, Ti, and Si substrates, seen in figure 2.2b, become chemisorbed and are unable to be removed. After the scotch tape removal, the only nanocrystal/substrate pairs that show chemisorbed adhesion, based on the XPS characterization, correspond to those with high oxidation potential surfaces where both the nanocrystals and substrates can participate in metal-oxide bond formation. Thus, no adhesion is observed for any pairs involving oxidized species, such as NiO nanocrystals or SiO_2 substrates. The potential outlier of the oxidized TiO_2 substrate showing adhesion can be understood as Ti/TiO_2 has multiple semi-stable oxidation states accessible to form metal-oxide bonds with the Ni nanocrystals and thus adhesion can be expected with the reactive Ni nanocrystals, but not with NiO nanocrystals. The combined XPS and SEM results suggest a potential adhesion mechanism by which Ni nanocrystals oxidize under ambient air conditions to form nickel oxide bonds with the substrate. This suggested mechanism is further supported by magnetic measurements addressed below.

Because the nanocrystals used in this work are superparamagnetic at room temperature, any observed non-zero coercivity could be resultant from interfacial stress due to bond formation with the substrate. [33] SQuID magnetometry measurements, figure 2.3, of the adhered Ni nanocrystals show the presence of out-of-plane coercivity, characteristic of an in-plane tension on the nanocrystals. The increased coercivity observed correlates with the degree of adhesion expected by SEM and XPS results, with the highest coercivity of 40.3 Oe, figure 2.3a, corresponding to the

nanocrystal/substrate pair with the highest oxidation potentials. Furthermore, the coercivity can be controlled by substituting in the less reactive substrate and nanocrystal surfaces of SiO_2 and NiO, reducing the coercivity to 24.6 Oe and 9.9 Oe, respectively, shown by figure 2.3.b, c. Thus, the magnitude of the out-of-plane coercivity can provide an indirect measure of metal-oxide bond formation and the degree of adhesion

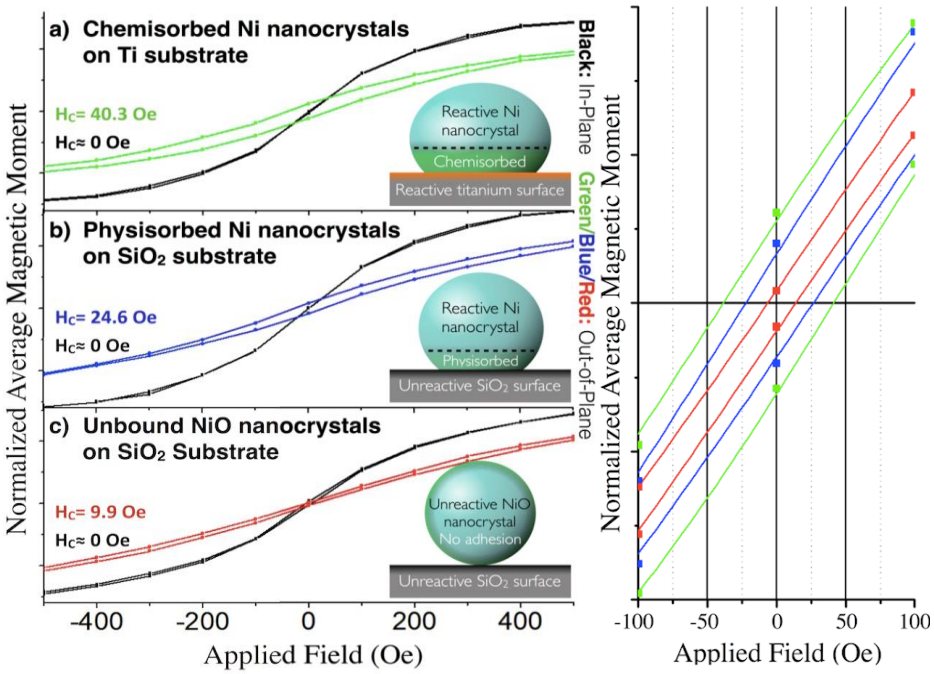

Figure 2.3. Room temperature magnetic hysteresis loops from SQuID magnetometry. Partial loop shown for clarity. (a) Strong adhesion of Ni nanocrystals on Ti substrate. (b) Weak adhesion of Ni nanocrystals on SiO_2 substrate. (c) No adhesion of NiO nanocrystals on SiO_2 substrate. Right graph shows coercivity trend of the three samples.

To fully demonstrate the oxidation adhesion mechanism is based on a metal-oxide bond formation, unadhered NiO nanocrystals on a Ti substrate were reduced back to reactive Ni nanocrystals enabling adhesion and then characterized by SQuID magnetometry. Control samples

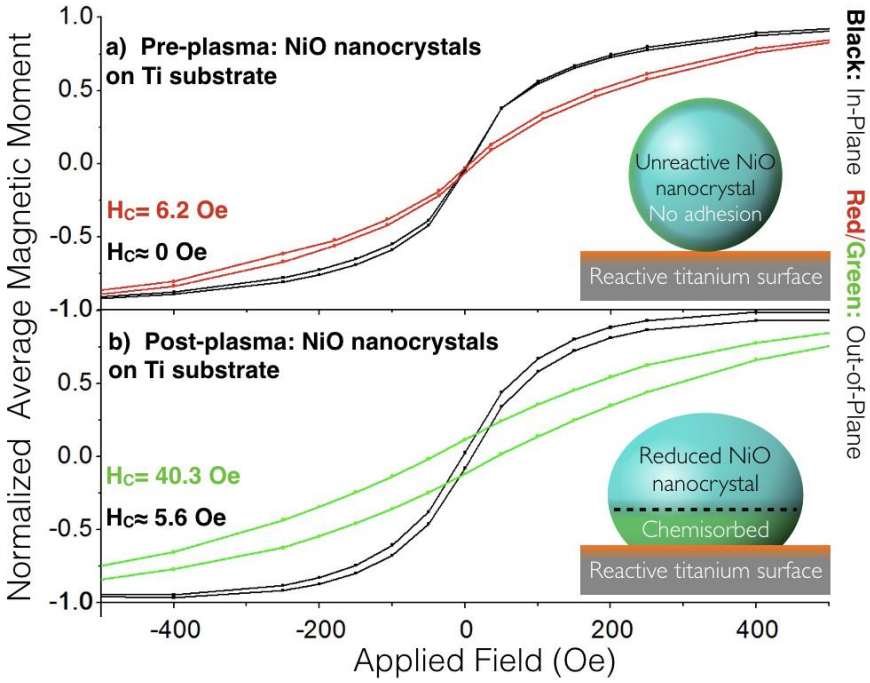

Figure 2.4. Magnetic hysteresis loops of (a) Unadhered NiO nanocrystals before plasma etching and (b) adhered NiO after reduction to Ni using reducing plasma.

of unbound NiO nanocrystals on a Ti substrate exhibit the expected low out-of-plane coercivity of 6.2 Oe, shown figure 2.4a. Fully adhered nanocrystals can then be induced by using reducing plasma (5% hydrogen, 95% argon) directly on this sample resulting in figure 2.4b, producing an out-of-plane coercivity of 40.2 Oe that is equivalent to the original benchmark sample for adhesion shown in figure 2.3a. By demonstrating reversible control over the oxidation adhesion process, there is strong evidence for oxidation at the nanocrystal/substrate interface playing a key role in the mechanism for adhesion of the nanocrystals.

Zero field cooled (ZFC) measurements using SQuID magnetometry of the normalized magnetic moments as a function of temperature show a 25 K shift in blocking temperature for adhered nanocrystals (blue) compared to unadhered nanocrystal (black), see figure 2.5. The

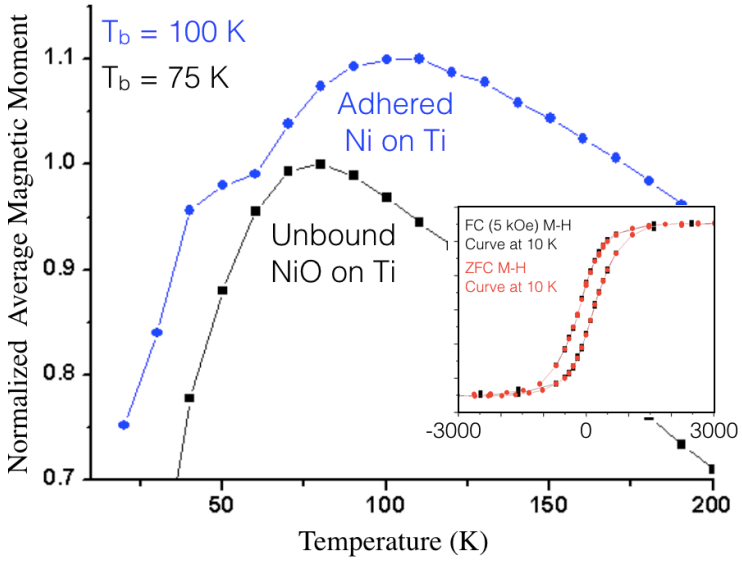

Figure 2.5. Zero field cooled magnetization curves of nanocrystals not adhered (black) and adhered (blue) with blocking temperatures of 75 K and 100K, respectively. Shoulder on blue curve from the presence of non-adhered nanocrystals. Normalized average magnetic moment (a.u.) versus applied field (Oe) of adhered samples show no exchange coupling present, see inset.

increase in blocking temperature for the adhered nanocrystals is expected due to the additional magnetic anisotropy from interfacial strain developed during adhesion. The shoulder observed for adhered nanocrystal sample indicates unadhered particles left from insufficient washing; however, this shows, due to adhesion, there is a clear dichotomy developed from an initially homogenous sample. As a final experiment, to rule out the possibility of an antiferromagnetic exchange bias from NiO affecting the magnetic anisotropy, ZFC and 5 kOe field cooled (FC) magnetic hysteresis loops were conducted at 10 K for the Ni nanocrystal/Ti substrate sample, see figure 2.5 inset. The inset shows the ZFC and FC hysteresis loops retrace completely, confirming no exchange bias is present in the samples and is in agreeance with literature findings. [34] Therefore, the increased

coercivity and blocking temperature of the adhered nanocrystals is in response to the interfacial stress generated during adhesion.

2.4. CONCLUSION

In conclusion, we have demonstrated a simple self-assembly based method to adhere magnetostrictive nanocrystals to various substrates through the formation of metal-oxide bonds at the interface. The oxidation adhesion process can be controlled by varying the reactivity of the nanocrystal/substrate interface and has been demonstrated to be reversible by using reducing plasma to induce adhesion of unadhered NiO nanocrystals. Adhered nanocrystals show an increased out-of-plane coercivity consistent with an in-plane tension from bond formation at the interface. With the development of the oxidation adhesion method, we will begin to explore nanocrystal-based strain-mediated magnetoelectric composites.

CHAPTER 3. ANISOTROPIC ELECTRIC FIELD CONTROL OF MAGNETIZATION IN A STRAIN-MEDIATED, NANOCRYSTAL-BASED MULTIFERROIC COMPOSITE

3.1. INTRODUCTION

Magnetoelectric composites represent a vast research field, encompassing many ferromagnetic and ferroelectric systems, with materials ranging from bulk ceramics to complex three-phase systems, and encompassing many different coupling mechanisms.[16, 35-37] The main feature of multiferroic composites is that they demonstrate a coupling between magnetic and

electrical degrees of freedom. This physical effect is quite important for various commercial applications.[35, 38-40] Among them are magnetic field sensors, power convertors, energy storing systems, cooling devices, etc. In most cases (excluding some recently proposed exotic mechanisms)[41-45] the coupling is dependent on a physical interplay between magnetoelasticity and piezoelectricity.[35] The general fabrication of such strain-mediated multiferroic composites consists of a magnetoelastic material deposited onto a piezoelectric substrate.[35, 46] With this composite material, an electric field induced piezoelectric strain can be transferred across the bonding interface to the magnetoelastic layer, resulting in a change to the system's magnetization and vice versa. Both computational and experimental studies have applied this approach in layered and patterned structures.[36, 47-61] As an example, Chavez et al[62] experimentally demonstrated a controllable 85% reduction in the saturation magnetization of patterned ferromagnetic disks using this strain-mediated approach. Such a design should also be applicable to magnetic nanocrystal systems, known as granular multiferroics, and that is the focus of this work.

Development of strain-mediated nanocrystal-based multiferroic materials, also termed granular multiferroics (GMFs), have the potential to complement previous studies by allowing for new control of many exotic magnetic properties that are common to nanoparticle systems. For instance, due to their strong ferromagnetic resonance (FMR), magnetic nanocrystals are interesting candidates for microwave absorbers, and strain-mediated control of magnetism in those systems could result in materials with a voltage tunable FMR frequency.[63-67] Strain-mediated magnetoelectric coupling in nanocrystal systems has been previously studied.[35, 68-78] However, most studies were motivated by magnetic sensor applications and the major figure of merit focused on the magnetoelectric coupling coefficient $\alpha_E = dE/dH$. That is to say, the goal was to optimize the electric field response induced by a magnetic field. However, the inverse effect of controlling

the magnetic state via an electric field needs further research. Kim et al[79] demonstrated this effect using a strain-mediated composite similar to ours, however the composite used ex-situ poling and required an irreversible phase change in the PMN-PT ferroelectric to generate a large one-time strain. Here, we utilize a cut of PMN-PT with biaxial strain, allowing for further exploration of the unique superparamagnetic properties of nanocrystals, all while remaining within the reversible linear region of the piezoelectric.

Here, we specifically utilize an *in-situ* applied voltage on a nanocrystal-based composite, composed of single domain Ni nanocrystals adhered to a (011) cut single crystal PMN-PT substrate. The PMN-PT substrate has an electric field induced biaxial strain response that can generate a reversible magnetic anisotropy in the Ni nanocrystals, which are otherwise in their superparamagnetic state, meaning they are magnetically isotropic. This type of strain state is advantageous since it provides a mechanism to control the direction in which the magnetization rotates due to the applied strains.[80-82] Specifically, for Ni, which is negative magnetoelastic, the magnetization rotates towards the axis of compressive strain. We observe this in our strain-mediated GMF composites as a shift in the blocking temperature of the nanocrystals. We also observe inverse responses when measuring the magnetization along the different biaxial strain axes.

3.2. EXPERIMENTAL

3.2.1. Ni Nanocrystal Synthesis. Nickel (II) acetylacetonate (Aldrich, Tech., 90%), Oleylamine (Aldrich, 70%), trioctylphosphine (Aldrich, 97%), oleic acid (alfa Aesar, Tech., 90%),

and 1-octadecene (Acros Org., Tech., 90%) were used in the preparation described here without further purification.

Synthesis of nickel nanocrystals followed a modified version of a method published by S. Carenco, et al.[29] The synthesis was carried out under an argon atmosphere using standard air-free techniques on a Schlenk line. Nickel nanocrystals were synthesized by the thermal decomposition of 1 mmol nickel acetylacetonate in the presence of ~18 mmol oleylamine (5.78mL), 1 mmol oleic acid (0.315 mL), 2 mmol trioctylphosphosphine (0.91 mL), and sufficient 1-octadecene to fix the total volume at 7 mL. On the Schlenk line, the solution was stirred while undergoing multiple pump/purge cycles for 30 minutes at room temperature and again at 90 ˚C for an additional 30 minutes to remove trace oxygen/water from precursors. The solution was then refluxed under inert atmosphere at 220 ˚C for 45 minutes, using a ramp rate of 15 ˚C/min to get to temperature, and then rapidly cooled to room temperature after completion. The nanocrystals were then purified by adding 1 mL hexanes and 40 mL of ethanol to precipitate the nanocrystals. A 25.4 mm N52 neodymium magnet was used to collect the nanocrystals, and to improve monodispersity, in place of the standard centrifugation methods. Samples were then resuspended in hexane and the cleaning process was repeated two additional times. The final solution was suspended in 20 mL of hexanes and used immediately.

Because the surface adhesion process used in this work involves an oxidative coupling of the nanocrystals to the titanium/titanium oxide surface, we also needed a non-adhered nanocrystal sample with a surface oxide to serve as a magnetic control. These were generated by sonicating the Ni nanocrystals for several hours under mild heating (40 ˚C) in a two-phase solution of ethanol/water and hexanes, until the nanocrystals transferred to the polar phase due to oxidation. The oxidized nanocrystals would be washed and purified and recharacterized.

3.2.2. PMN-PT. The single crystal PMN-PT $[Pb(Mg_{1/3}Nb_{2/3})O_3]_{0.68}[PbTiO_3]_{0.32}$ substrates used in this work was purchased from TRS Ceramics (TRS X2B d32 plates, dimensions 20 x 10 x 0.5 mm). The substrate has an electric field dependent compressive strain along the (100) in-plane axis and a tensile strain along the (011-) in-plane axis. Along the (011) out-of-plane axis there is a tensile strain response with an electric field. Substrates were cut to 4 x 4 x 0.5 mm dimensions for in-situ poling in the SQuID magnetometer.

3.2.3. Fabrication of the GMF composite. Adhesion of Ni nanocrystals uses the simple self-assembly based method described in chapter 2 that produces covalent bonding between the nanocrystals and a titanium bonding interface. In general, to adhere nanocrystals to the piezoelectric, 25 nm of Ti was sputtered onto the PMN-PT as the bonding interface. The reactive PMN-PT/Ti substrate was immediately submerged into a solution of newly synthesized Ni nanocrystals under ambient conditions. The unoxidized nanocrystals were allowed to react with the Ti surface layer to form a strong metal oxide bond to the substrate. After adhesion of the nanocrystals was completed the substrate was cleaned with multiple cycles of hexane rises and sonication to remove any unadhered nanocrystals. Control substrates were used to confirm the quality of the monolayer as a final step. To add electrodes, the substrate was first etched using an Ar plasma to remove organic ligands on the nanocrystals and then, without breaking vacuum, a Pt layer (20 nm) followed by a subsequent Au layer (50 nm) was deposited via sputter deposition. A 50 nm Au layer was later deposited on the reverse side of the PMN-PT substrate as a counter electrode.

The Pt and Au layers serve to prevent further oxidation of the nanocrystals and to create a uniform electric field across the PMN-PT. They may also contribute to the strain transfer between the PMN-PT substrate and the nanocrystals, but the primary strain transfer occurs via the covalent

adhesion between the Ni nanocrystals and the titanium oxide top surface of the substrate. This claim is based on numerous efforts to induce strain transfer to nanocrystals using a broad range of nanocrystal samples, surface chemistries, and capping layers. From this work, we found that strain transfer requires chemical adhesion of the nanocrystals to the substrate and a Pt or Au coating alone was insufficient to create strain transfer.

3.2.4. Measurement. The strain response of the PMN-PT single crystal substrates was measured using a biaxial strain gage from Vishay Precision Group. The substrate is cleaned using acetone, methanol, and then IPA and subjected to a 60 s 100 W O_2 plasma clean. Ti(5 nm)/Au(100 nm) electrodes are deposited by e-beam evaporation on the top and bottom surfaces of the substrate. Following the deposition, the strain gage was adhered to the top surface with M-Bond 200 adhesive and then placed in a 1 cm x 1 cm chip carrier to add the wire bonds. The electric field was applied using a voltage amplifier and ranges between 0 MV/m to 0.8 MV/m. The strain data is collected using a National Instruments DAQ device.

Magnetic measurements were conducted using a Quantum Design, MPMS XL-5 superconducting quantum interference device (SQuID) magnetometer operating in VSM mode. Scanning electron microscope (SEM) images taken via JEOL JSM-6700F FE-SEM. Powder X-ray diffraction patterns were measured using a PANalytical X'Pert Pro using a Cu Kα (λ = 1.5418 Å) source, operating at 45 kV and 40 mA. XRD patterns were recorded in the range of $30° < 2\theta < 60°$.

3.2.5. Modeling. We performed Monte-Carlo simulations of the strain-mediated GMF system. Due to the complexity of self-assembled systems, we focused on a simplified model to gain a better understanding the trends of the system. We do not consider the precise magnetization

of the Ni nanoparticles and their specific anisotropy, as these depend on the details of the oxidation that takes place during the adhesion process. We also do not take into account the randomness of particles positions and other similar effects. As a result, we do not have perfect fits to the experimental magnetization curves across the whole temperature range. However, we can still understand many of the more important trends from our modeling.

To understand the behavior of magnetic grains in the hybrid nanocrystal/ferroelectric system, we use Monte-Carlo simulations. We describe our particles with the following Hamiltonian:

$$H = -\sum_i \lambda_i (\mathbf{m}_i \mathbf{n}_i)^2 + \sum_{ij} M_i M_j \left(\frac{(\mathbf{m}_i \mathbf{m}_j)}{|\mathbf{r}_{ij}|^3} - \frac{3(\mathbf{m}_i \mathbf{r}_{ij})(\mathbf{m}_i \mathbf{r}_{ij})}{|\mathbf{r}_{ij}|^5} \right) + E_{me}, \qquad (1)$$

where $\mathbf{m}_i$ are the unit vectors co-directed with i particle magnetization, M_i is the particle magnetic moment (using bulk Ni magnetization of about 450 Gs). Here λ_i is the uniaxial anisotropy constant (we take $1.4*10^5$ erg/cm^3, which is close to values reported in the literature[83]). The anisotropy axes $\mathbf{n}_i$ are randomly distributed over all possible directions. We assume a log-normal size distribution of the particles with dispersion σ_d. The average size of the particles can be estimated from the TEM image as 15 nm. While they physical size distribution could be estimated from our TEM data as well, we use the dispersion term to capture the distribution of anisotropy energies of the particles, and those anisotropies depend on shape, surface structure, and the details of the bonding to the substrate in addition to size, and so we use this term as a fitting parameter. Finally, $\mathbf{r}_{ij}$ is the vector connecting particles i and j.

Based on our preparation procedure, the grains should form a single layer on the piezoelectric substrate. Therefore, in our modeling we also use this geometry as well, and for

simplicity assume a square lattice. In reality, our TEM images show more or less random distribution of particles, but based on additional modeling, different types of particle arrangements do not give qualitatively different results. The average distance between the particles is estimated of 5 nm according to the TEM images. The last term E_{me} describes the strain-mediated magnetoelectric coupling in our system. We assume that when we apply an electric field to the PMN-PT substrate, we induce a strain. This strain is transferred to the ferromagnetic particles. This, in turn, induces additional magnetic anisotropy in each particle due to the magnetoelastic effect. Therefore, we add the following term to the Hamiltonian

$$E_{me} = -\sum_i \lambda_{ind}(\mathbf{m}_i \mathbf{n}_{ind}),^2 \qquad (2)$$

where λ_{ind} is the magnitude of the induced anisotropy. It linearly grows with strain and therefore with electric field. The induced anisotropy is uniaxial, with the direction of the anisotropy defined by the main axes of the PMN-PT crystal. Generally, bulk Ni has a negative magnetoelastic coefficient, meaning that the anisotropy decreases along the compression direction. When we apply the electric field, the compression appears along the (100) direction and $\mathbf{n}_{ind}||(100)$.

We then follow a standard approach in which at each Monte-Carlo step we randomly choose a magnetic particle and randomly rotate its magnetic moment. Maximum deviation of the magnetic moment is chosen to obtain a reasonable acceptance rate. Acceptance probability is 1 if the energy of the new system state is less than the energy of the old state. The acceptance probability is $\sim e^{-\Delta E/k_B T}$ if the energy difference between the new and old state ΔE is positive. Using the Monte-Carlo approach we calculate the dependencies of the system's coercive field on temperature T. More details on the simulation proceed can be found in the Appendix section.

3.3. RESULTS AND DISCUSSION

3.3.1. Materials Characterization. With the goal of mechanically straining magnetic nanocrystals with a piezoelectric material, it is important to start with well-defined magnetic and piezoelectric properties, as well as have a strong mechanical coupling between the two components. Unless these criteria are met, it will be hard to observe changes in magnetization, either because signals will be too broad or they will be nonexistent due to insufficient strain transfer.

Solution processed methods were used to synthesize monodispersed Ni nanocrystals with a 14 nm diameter, as seen in the SEM images in figure 3.1, inset. Powder XRD of was used to confirm that the correct crystal phase was synthesized. These small nanocrystals are ideal as they will not only require less mechanical strain to modify their magnetic properties, but they also have a higher surface energy, which is needed to chemically adhere the nanocrystals to the piezoelectric substrate.

Based on previous the work in Chapter 1, a monolayer of Ni nanocrystals can be chemically adhered through covalent bonding to surfaces with a high oxidation potential, such as titanium/titanium oxide. The mechanism of adhesion relies on the reactive surface energy of the metallic nanocrystals and the formation of metal-oxide bonds at the interface. A monolayer of self-assembled Ni nanocrystals adhered to a titanium sputtered silicon wafer is shown in the inset of figure 3.1. The nanocrystal monolayer can be seen to be nearly complete with no signs of multilayers. This is important because strain transfer occurs directly from the substrate to the covalently attached nanocrystals, so any multilayer nanocrystals will not be strained.

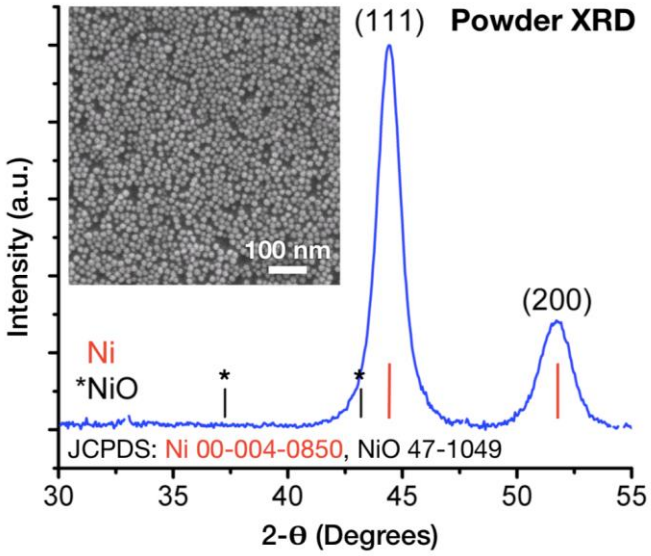

Figure 3.1. Representative powder XRD of the Ni nanocrystals used for this work. The data confirms that samples have the correct crystals phase and the diffraction shows no evidence of significant oxidation. The inset shows an SEM shows a uniform monolayer of monodispersed 14 nm Ni nanocrystals.

Because the adhesion is based on metal-oxide bond formation, the Ni nanocrystals will develop an isotropic in-plane tensile strain upon adhesion, which can be observed by an increased out-of-plane coercivity. This isotropic strain will be added to any additional strain introduced during poling of the piezoelectric material. In figure 3.2, SQuID magnetometry results confirm this in-plane tensile strain as a difference in the out-of-plane coercivity for unadhered and adhered nanocrystals. Note that the unadhered samples were also allowed to develop a thin, self-limiting surface oxide, so the difference in these magnetic results are not due to surface oxidation or exchange coupling to an antiferromagnetic NiO_x surface layer. At 298 K, the H_C is 0 Oe and 65 Oe

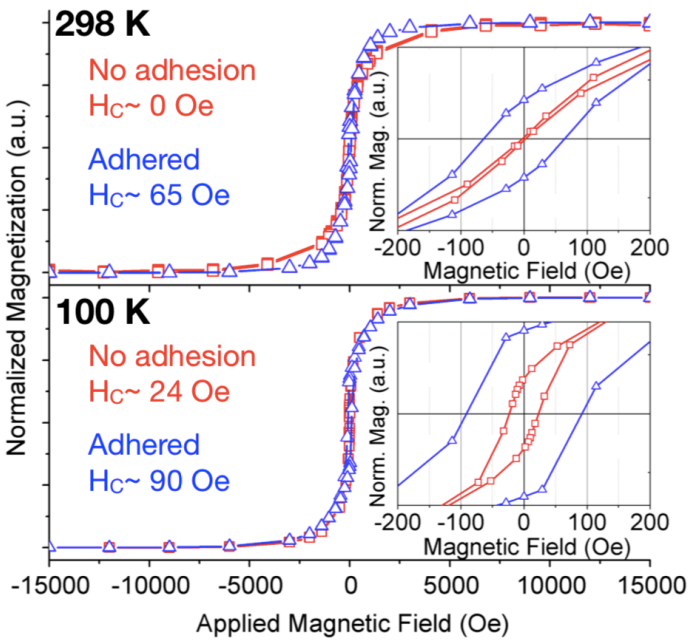

Figure 3.2. Normalized out-of-plane M-H loops for nanocrystals with no adhesion (surface oxidized in solution and then spin coated monolayer on SiO_2 wafer, red lines), and nanocrystals that are covalently bonded to the substrate (chemically oxidized onto a PMN-PT/Ti/TiO_x wafer, blue lines), collected at both 298K and 100K. Data collected at lower T shows increased coercivity, but the difference between the two samples remains constant.

for the unadhered and adhered samples, respectively; at 100 K, these H_C values increase to 24 Oe and 90 Oe. The unadhered samples are SPM at 298 K (H_C = 0 Oe), while the adhered nanocrystals are ferromagnetic at this temperature due to the additional isotropic strain developed during adhesion. Only at lower temperatures do the unadhered nanocrystals show non-zero coercivity. This difference in coercivity confirms successful chemical adhesion to the Ti/PMN-PT wafer that should allow for efficient strain transfer from the piezoelectric material to our magnetoelastic nanocrystals.

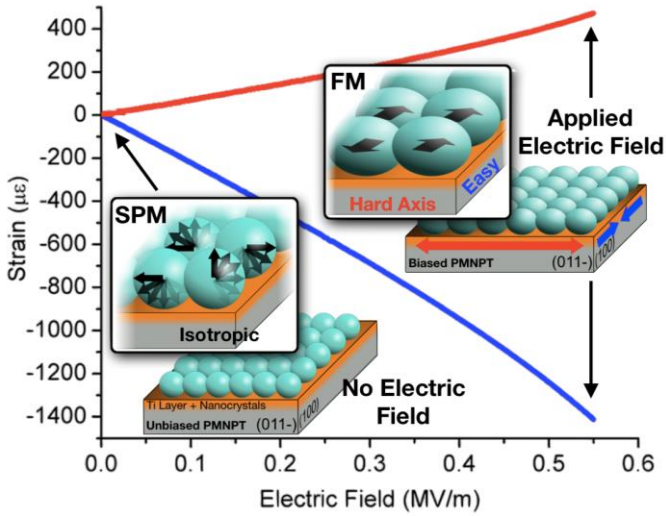

Figure 3.3. Strain response of PMN-PT as a function of electric field. The (100) axis develops a compressive strain, while the (011-) axis develops a tensile strain. Cartoon schematics of Ni nanocrystals adhered to the Ti/PMN-PT substrate. Unstrained the nanocrystals are magnetically isotropic, however under strain, the magnetic moments develop an easy and hard-axis, corresponding to the (100) and (011-), axes respectively.

Characterization of the strain response of the PMN-PT single crystal substrates was measured using a biaxial strain gage from Vishay Precision Group applied to a sister substrate. The PMN-PT substrate has an anisotropic strain in the (100) and (011-) axes, as shown in figure 3.3. The (100) axis, shown in blue, experiences a large compressive strain of roughly 1400 με at 0.55 MV/m. Whereas, the (011-) axis, shown in red, experiences a much smaller tensile strain of roughly 400 με at 0.55 MV/m. Two cartoon schematics are provided in figure 3.3, showing nanocrystals adhered to the Ti/PMN-PT substrate, with and without an applied bias. When unbiased, the nanocrystals are shown to be SPM with no magnetic easy-axis (magnetically isotropic) and the magnetic moments are dynamically flipping as a result of thermal fluctuations. When the PMN-PT is biased, the introduced anisotropic strain causes the nanocrystals to go from

being magnetically isotropic to anisotropic. Because Ni has a negative magnetoelastic coefficient, the axis along the compressive (100) axis of the PMN-PT is shown to become the magnetic easy-axis and the axis along the tensile (011-) axis of the PMN-PT becomes magnetically hard. The scenario this cartoon shows is assuming an idealized temperature range, where the additional magnetic anisotropy introduced by the magnetoelastic effects is not masked by thermal energy. It also depicts the scenario with no applied magnetic field, hence we show a random distribution of spin up/down magnetic moments along the (100) axis. We also note that while nanocrystals should couple in ferromagnetic chains along the (100) direction if there is an applied magnetic field, the magnetic alignment without an external magnetic field would depend on neighboring chains and could show ferromagnetic or antiferromagnetic coupling. In either case, the (100) axis is shown to be favorable.

3.3.2 Voltage dependent magnetic response. Zero field cooled (ZFC) curves of the strain-mediated granular multiferroic (GMF) composite were measured using SQuID magnetometry, as shown in figure 3.4. In this experiment, the sample was first biased, and then cooled to a low temperature. Here, we went to 50K for the (100) and 20 K for the (011-) data. The final temperature was chosen to minimize thermal shock to the sample so that expensive PNM-PT substrates could be reused, while still enabling data collection in the region of interest upon warming. A maximum bias of 375 V was applied in-situ along the out-of-plane (011) axis, and the changes in magnetization in both the easy (100) and hard (011-) axis were measured. Along the easy-axis, where the sample experiences compression, the blocking temperature (T_b) can be seen to increase from 50 K, unbiased, to 120 K when biased to 375 V. The shift in the easy-axis T_b toward higher temperatures indicates the compressive axis has become energetically favorable for magnetic moments; it has evolved into a deeper energy well because strain anisotropy is adding to

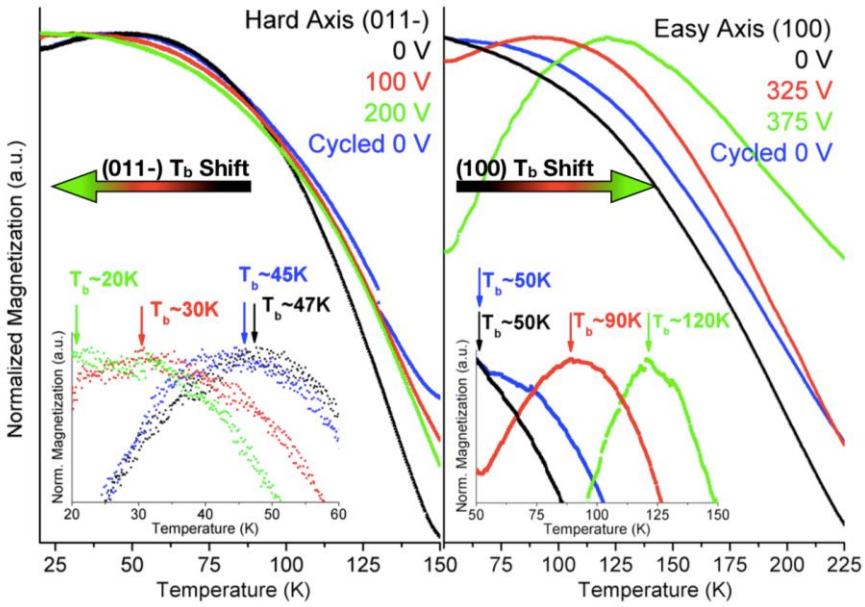

Figure 3.4. Normalized ZFC curves as a function of applied voltage, where compression in the (100) axis, shifts T_b to higher T, and tension in the (011-) axis, shifts T_b to lower T. The insets show the data on an expanded y-scale to make the shifts easier to see. The shifts in T_b with voltage go in opposite directions due to the anisotropic strain. Cycled 0 V data show that changes are reversible and the strain can be released after the applied bias is removed.

the existing nanocrystal anisotropy and so a greater thermal energy is needed to randomize spins pointed in this direction. Along the (011-) hard-axis, where the sample experiences tension, T_b can be seen to decrease from 47 K, unbiased, to 20 K, when biased to 200 V. The shift in the hard-axis T_b, toward higher temperatures indicates that this tensile axis has become energetically unfavorable for magnetic moments. In other words, spins aligned in this direction experience a shallower energy well because the strain anisotropy is canceling the initial nanocrystal anisotropy, and so it takes less thermal energy to randomize them. For both the easy and the hard axis, an unbiased measurement (0 V Cycled) is made after biasing, showing that T_b mostly returns to its original, unstrained, value. A noticeably higher applied voltage is required for the easy-axis to

show any initial shift in the easy-axis T_b compared to the hard-axis. This is most likely due to the fact that the nanocrystals are already under tension, as discussed in figure 3.2 above, developed during the adhesion process.

Above we discuss the easy-axis T_b and hard-axis T_b, defining these terms as the inflection point in the ZFC curve, as is standard for nanoscale magnetic materials. We need to point out, however, that the hard-axis T_b is not a true blocking temperature, as a blocking temperature implies a transition temperature from a fixed or ferromagnetic state, to a randomized, fluctuating or superparamagnetic state. The decrease in magnetization above a true T_b is due to randomization. For the hard-axis data presented here, once spins are able to escape their potential well, there is another, deeper well that becomes accessible to them. As a result, the decrease in magnetization at temperature greater than the "hard-axis T_b" is attributed to the magnetic moments transitioning to the more stable (100) easy-axis and not to the randomization of the magnetic moments. The (011-) axis can be thought of as a metastable state, where the depth of the potential well is due to the competing energies from the intrinsic nanocrystal anisotropy and the applied strain field. As we vary the magnitude of the strain field with voltage, we vary the depth of this well and the thermal energy needed for spins to escape to the truly stable state of the system, i.e. aligned along the compressed (100) easy-axis.

We note that for figure 3.4, the shift in the hard-axis T_b is limited by the low starting temperature. To resolve this, we allowed the adhered nanocrystals to oxidize in open air for an extended period of time. From previous experience, this is a simple way to increase the overall magnetic anisotropy of nanocrystals due to increased pinning of surface NiO_x spins. For this partly

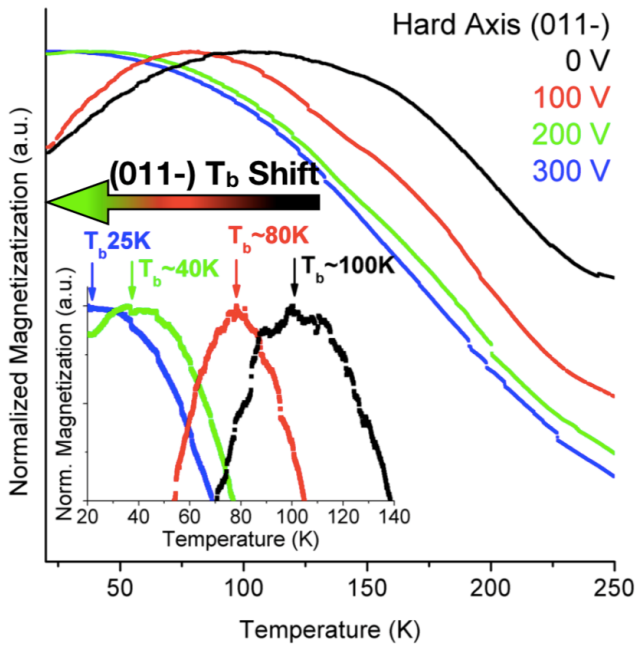

Figure 3.5. Normalized ZFC curve as a function of applied voltage for the (011-) axis. The applied voltage leads to tension in the (011-) axis, which shifts T_b to lower T. The inset again show the data on an expanded y-scale to make the shifts easier to see. The higher initial blocking temperature for this sample allows for larger shifts and thus better characterization of the ability for an applied voltage to reduce the hard-axis T_b.

oxidized sample, the unpolled blocking temperature increases to 100K. Data for the hard-axis T_b as a function of voltage for this sample is shown in figure 3.5. The hard-axis T_b can be seen to decrease from 100 K, unbiased, to 25 K when biased to 300 V. This is a significantly larger shift than in the first measurement and provides a clearer picture of the extent of tuning that is possible. Easy-axis data was not collected on this sample because shifts would exceed the upper temperature limit of our system.

The overall trends of shifts in the easy-axis and hard-axis T_b (shown in figure 3.4 and figure 3.5) are modeled in figure 3.6 using Monte-Carlo simulations. Similar to our experimental

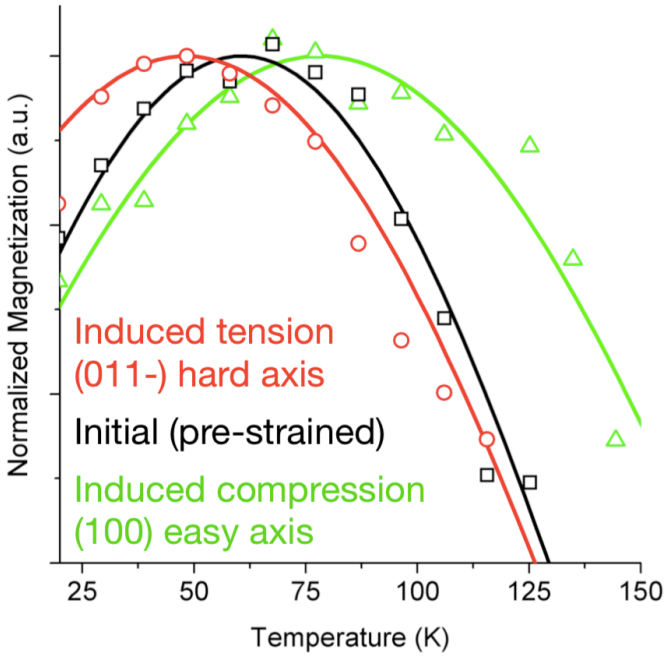

Figure 3.6. Monte Carlo simulation of the strain-mediated GMF composite. From the initial (pre-strained) state an induced tension and compression produces the observed experimental trends.

observations, when we apply the electric field in our model, we observe a decreased anisotropy along the (100) direction. Solid lines are a guide for the eyes. As a note, our model requires the system has some initial uniaxial strain in the (100) axis in order to observe trends similar to the experimental data. Without the initial strain our model gives increasing of temperature of ZFC peak for both directions (100) and (011-). This is probably related to the fact that behavior of the peak position is non-linear and non-monotonic with strain. The weak strain moves both peaks to the same direction, but higher strain moves one peak to higher temperature but another peak to lower temperature. With this initial strain present, the peak of the ZFC curve for magnetic field along the (100) moves to higher temperatures, while for the (011-) axis the peak shifts to lower temperature. The exact nature of the initial strain needs further investigations, but, it is well

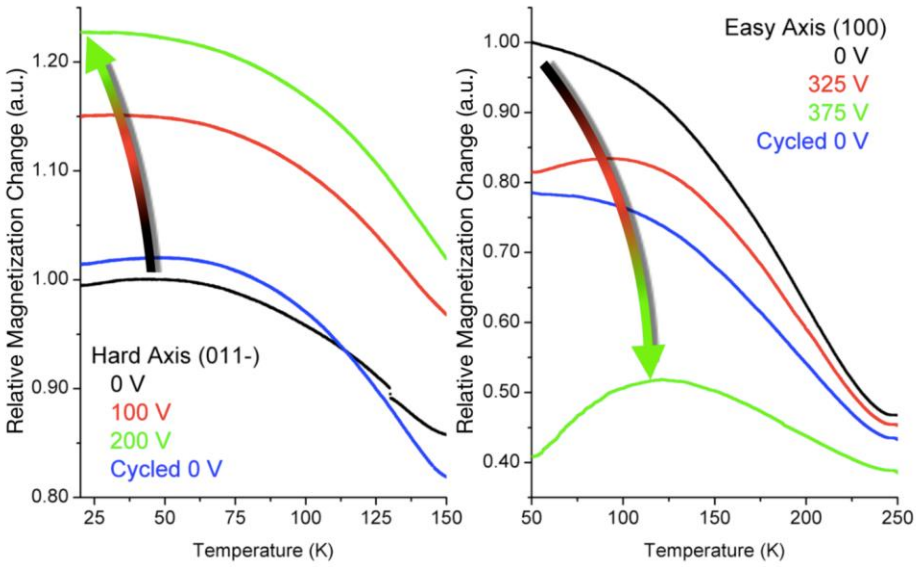

Figure 3.7. The relative magnetization change as a function of voltage shows increasing magnetization along the (011-) hard-axis, and decreasing magnetization along the (100) easy-axis. When the applied bias returns to 0 V, the magnetization mostly returns to its original state, although some residual strain is observed in the (100) easy-axis direction.

established thermal expansion should be dependent on crystal direction. As a result, it is not unreasonable to assume that some anisotropic strain develops, either during cooling or during the oxidative chemical adhesion of the nanocrystals to the substrate.

We now go back to the experimental data, this time focusing on the relative change in magnetization for the easy and hard axes. Here again we see that the two axes response in opposite ways to an applied voltage, as seen in figure 3.7. The magnetization at the peak of the curve (T_b) increases by about 23% with an applied bias in the hard-axis (011-) direction, while the peak magnetization in the easy-axis direction decreases by about 49% with an applied bias. The two samples were fabricated from the same batch of nanocrystals and piezoelectric substrate. However, to account for small variations in sample adhesion and monolayer coverage, the magnetization per

composite area was normalized by setting the starting unbiased magnetization at 50 K equal for both samples. The voltage dependent trends in magnetization of the two axes at first seems counter intuitive, but can be understood by considering the sequence of measurement and biasing. The samples were biased throughout the entire sequence of a standard ZFC measurement. This means, the electric field was first applied at room temperature, and then it was held constant as the sample was cooled under zero applied magnetic field and as it was subsequently heated under a small magnetic field during the measurements. From figures 3.4 and 3.5, it is clear that an applied bias creates a preferred potential for magnetic orientation along the compressed (100) easy-axis. However, because the biased sample is cooled from room temperature without an applied magnetic field, the magnetic moments in this easy-axis direction distribute with equal probability in the spin up and spin down direction. This causes most of the spins along the easy-axis direction to cancel. Note that spin cancelation occurs between nanocrystals, not within a single nanocrystal. When the sample is cooled, these spins become locked in this low magnetization configuration and cannot align with the small applied magnetic field used for measurement upon warming in the ZFC experiment. This leads to the observed behavior in figure 3.7, where a larger voltage causes a greater number of magnetic moments to cancel, and thus a smaller overall magnetic moment is measured at lower temperatures along the easy-axis. As the temperature is increased, the sample loses memory of this initial state and the magnetization for all samples becomes more similar.

The reverse follows for measurements along the (011-) hard-axis (figure 3.7). Here, the potential well becomes shallower with increasing initial bias, and so fewer spins are locked into a canceling configuration. As a result, the small bias used for measuremnt is enough to align a much larger fraction of the nanocrystal spins in the sample along the measurement axis. The highest magnetization corresponds to the shallowest potential well and the highest applied bias.

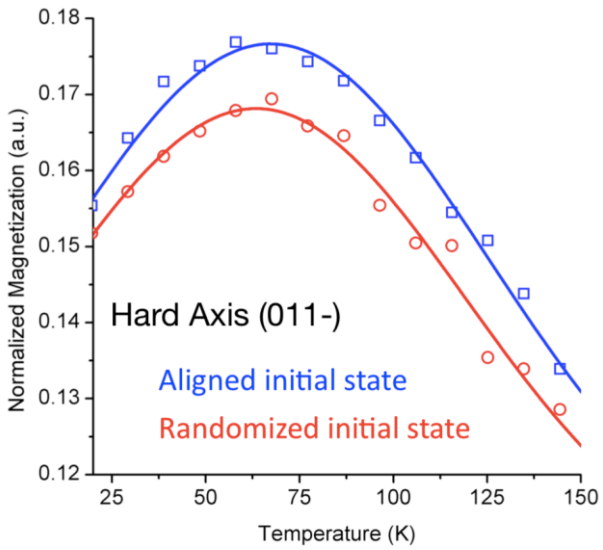

Figure 3.8. Monte-Carlo simulation of ZFC curves measured along the (011-) axis, with different initial magnetic states. Blue curve, represents a system starting with magnetic moments aligned along the (100) axis, i.e. a strained system. Red curve, represents a system starting with magnetic moments randomized, i.e. an unbiased system. The modeled system suggests the initial magnetic orientation prior to heating and measurement influences the relative change in magnetization observed experimental. Lines are provided as guides for the eyes.

In essence, our claims above suggest that the initial alignment of the magnetic moments in our system are responsible for the observed trends in increasing and decreasing magnetization. Investigation of this claim is challenging as the initial state is of course not something that can be probed experimentally, since measuring the initial magnetic state would by the very act, disrupt it. Instead, we rely on a simplified Monte-Carlo model to compare two systems with different initial magnetic alignments, being either fully aligned along the (100) axis or being fully randomized. The typical ZFC curves resulting from the two initial states simulated are show in figure 3.8. The ZFC curves simulated correspond to measurements made along the (011) axis. From the

simulations we see similar trends as observed experimentally (compare with figure 3.7, hard axis data), where the simulated ZFC curves with a (100) aligned initial state, blue, shows an increased magnetization compared to the randomized initial state, red. The reason for the difference appears due to the fact that relaxation of magnetic moments during the heating is different since we start with different initial state. This however should strongly depend on the ratio between measurement time and particle relaxation time. There may be a rather strong dipole-dipole interaction the system relaxation is slow (as in spin glasses), therefore it cannot relax in the same manner when starts from different initial states. This Monte-Carlo simulation provides strong support for the assumptions made for our experimental observations, highlighting the behavior of the initial magnetic state in our system, which cannot be experimentally investigated.

To confirm these ideas, we perform further experimental studies to show this trend in relative magnetization can be eliminated by applying the electric field only during the heating sequence of the ZFC measurement, figure 3.9. By applying the electric field only after cooling has finished and just prior to applying the magnetic field for measurement, the magnetic moments should have fully randomized orientations at the start of heating and measurement. This is because by time the electric field is finally applied, the magnetic moments at this cryogenic temperature are in a blocked, ferromagnetic state and should not have sufficient energy to reorient in response to the strain. Furthermore, the piezoelectric response at cryogenic temperatures is significantly lowered compared to the room temperature response.[84] Thus, we see that the unnormalized ZFC curves show almost no change in magnetization with an applied voltage, as shown in figure 3.9a. From the normalized graphs (figure 3.9a, inset), the expected trend for the easy-axis T_b shift is still observed, however the shift is much smaller due to the smaller cryogenic piezoelectric strain response. To summarize all this data, the relative percent change in peak magnetization for samples

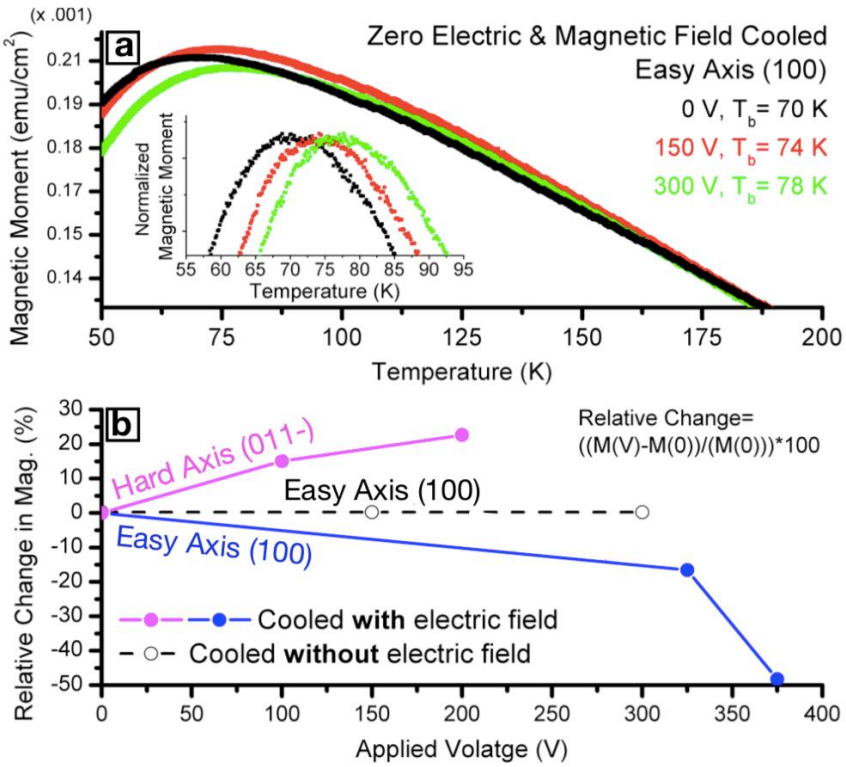

Figure 3.9. (a) ZFC measurements along the (100) easy-axis for a system cooled without an applied electric field. The data show a voltage dependent shift in the hard-axis T_b (see inset for normalized data with an expanded y-scale), but the change in magnetization with voltage is very small and shows no trend with bias strength. (b) Comparison of the relative change in peak magnetization for systems cooled with and without an applied electric field. When cooled with an electric field the hard and easy axes show divergent changes in magnetization intensity with an applied bias, while when cooled without an electric field there is essential no change.

cooled with and without an electric field is shown in figure 3.9b. The easy and hard-axis magnetization changes for samples cooled with an electric field have opposing trends with an applied voltage. However, when the easy-axis is cooled without an electric field, the peak magnetization shows effectively no change. While many of the general trends in this data can be easily understood, we note that further experimentation is still needed to fully understand this

behavior, as there are likely other factors that can explaining the smaller differences noted for the various ZFC sequences. For example, one possible reason for some of the differences could be the different strain profiles developed during cooling with and without an electric field. Overall, however, the data in figure 3.9 not only confirms our explanation of the trends observed during the various ZFC measurements, but it also further demonstrates our ability to control the magnetization in superparamagnetic nanocrystals with an applied voltage.

3.4. CONCLUSIONS

In this work, we fabricated a composite multiferroic system with a single layer of magnetic Ni nanocrystals placed on top of a piezoelectric PMN-PT substrate. Using oxidative chemical adhesion, we obtained mechanical coupling between the nanocrystals and the piezoelectric substrate. We then applied an electric field to the PMN-PT substrate and measured the magnetic properties of the Ni nanocrystals using SQuID magnetometry. Strain-mediated magnetoelectric coupling occurred in the system and we found that the blocking temperature of the magnetic particles could be changed using an electric field. We specifically found that the anisotropic in-plane strain of the piezoelectric substrate could be used to create reversible magnetic anisotropy in the nanocrystals, with the apparent blocking temperature moving to lower temperature in the magnetic hard-axis, and to higher temperature in the magnetic easy-axis. Changes in the extent of spin cancelation between nanocrystal, and thus changes in the overall sample magnetization, could also be controlled by changing the specific sequence of when the electric field was applied (either before or after cooling the sample).

While this is a fundamental study with no specific applications, the combination of anisotropic strains, variable temperature, and the thermally activated fluctuations of a superparamagnetic material provide for a magnetic system that is highly tunable in many different ways. Most of the changes described here took place well below room temperature, but the entire temperature range for these phenomena can be shifted to higher values simply by increasing the size of the Ni nanocrystals. Such materials could eventually find applications in electric field modified magnetic read and write systems, where an electric field is used to dynamically reduce the magnetic anisotropy during write operations so that the same magnetic field strength could be used to both read and write. The tunable blocking temperature could also find potential applications in microwave filters. Regardless of the eventual application, this work adds to our understanding of how nanocrystals can be incorporated into anisotropic multiferroic composites.

CHAPTER 4. TUNING EXCHANGE COUPLING IN A NEW FAMILY OF NANOCRYSTAL-BASED GRANULAR MULTIFERROICS USING AN APPLIED ELECTRIC FIELD

4.1. INTRODUCTION TO GRANULAR MULTIFERROIC COMPOSITES

Magnetoelectric composites offer a unique way to control magnetism at the nanoscale by combining multiple materials properties into one composite. Conventional strain-mediated magnetoelectric composites use a piezoelectric layer that is mechanically coupled to a magnetostrictive magnetic layer [85-89]. This configuration allows an applied electric field to produce a strain in the piezoelectric, which is translated to the magnetic material of the composite to change its magnetic state. The ability to control magnetism via an electric field has led to many new

applications, such as energy efficient memory storage and logic devices [90-92], novel subwavelength antennas [93, 94], nanomechanical devices [95] and even magnetic tomography [96]. More complicated composite geometries have also been developed with magnetic nanocrystals being embedded into a ferroelectric matrix [68, 69, 97-100]. The higher interfacial area in these composites is appealing to strain-mediated multiferroic applications, promising enhanced coupling.

Recently, a unique mechanism of magnetoelectric coupling was proposed for nanocrystal-based or granular multiferroic (GMF) composites [41-44]. In this theoretical work, superparamagnetic nanocrystals were placed in close proximity to, or encased in, a ferroelectric matrix with a tunable dielectric constant. The mechanism to control magnetization in this new type of GMF composite relies on exchange coupling between nanocrystals, rather than on the standard mechanism of mechanical strain transfer. The extent of exchange coupling depends on the orbital wave function overlap between neighboring nanocrystals. Thus, exchange coupling between nanocrystals can be controlled in two ways: either (1) by varying the tunneling distance between nanoparticles or (2) by altering the nature (dielectric constant) of the tunneling medium between grains. For the second case, this dielectric can be tuned using a ferroelectric material whose dielectric constant can be changed by an electric field. This is thus a new mechanism for electric field control of the magnetic properties of a nanocrystal ensemble. Simulations show that this method can be used to tune the blocking transition temperature between superparamagnetic and ferromagnetic states, coercive field, and magnetic susceptibility of GMF composites.

As shown in figure 4.1, the dependence of nanoparticle coupling on the dielectric environment comes from the Coulomb blockade effect and from screening of inter-electron Coulomb interactions and thus modification of the potential barrier for electron exchange. Strong coupling leads to inter-particle magnetic ordering and ferromagnetic behavior, while weak

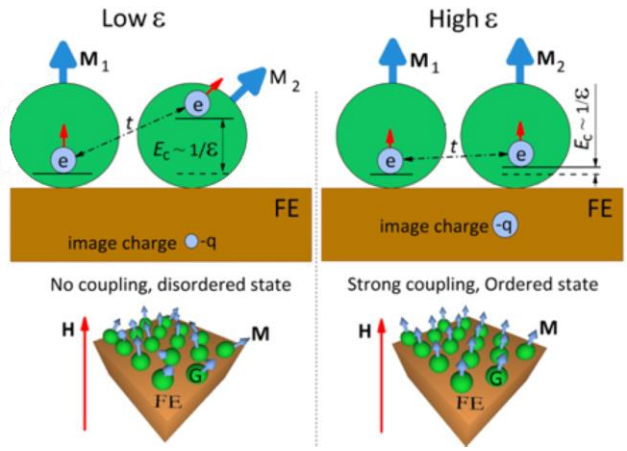

Figure 4.1. Cartoon showing the influence of the dielectric constant of a ferroelectric matrix, FE, on inter-particle exchange interactions (J) in GMF composites. The upper panel shows two interacting magnetic grains with magnetic moments $M_{1,2}$. Interaction occurs via virtual hopping of electrons (e) between grains with probability t. In a nanocrystal system, electron hopping is suppressed due to the Coulomb blockade effect, creating a gap, E_c. The exchange coupling can be roughly described as $J \sim t^2/E_c$. The Coulomb gap strongly depends on the dielectric constant of the surrounding media due to screening of image charges. When the dielectric constant is low (left panel) the gap is large and hopping (exchange) is suppressed, resulting in a disordered (superparamagnetic) magnetic state with no long-range order (bottom left). In contrast, strong exchange coupling occurs when the dielectric constant is high (right panel) resulting in an ordered (ferromagnetic) state with long-range ordering (bottom right).

coupling results in a disordered or superparamagnetic state. We note that this Coulomb blockade effect only appears in granular systems, and so this type of coupling does not occur in multilayer systems.

According to the theoretical modeling, magnetoelectric coupling for GMF composites is efficient only when the following conditions are satisfied: 1) the dielectric constant of the

ferroelectric component should be low (of order of 100); 2) magnetic grains should be metallic; 3) the grain size should be on the order of 10 nm; 4) the inter-grain distance should be on the order of 1 nm. In the literature, most nanoparticle-based composites do not satisfy these conditions, as they are fabricated using high-dielectric constant materials such as $BaTiO_3$ or lead zirconate titanate, which are optimized to produce large strains. Moreover, the grain size is generally large, and in many cases the grains are fabricated from ferrimagnetic insulators, such as $CoFe_2O_4$.

In this work, we fabricate for the first time a multiferroic composite that is optimized for exchange-based multiferroic coupling. We use a densely packed ensemble of metallic superparamagnetic nanocrystals and a ferroelectric material with a low-dielectric constant. Solution processed methods were used to synthesize the superparamagnetic nickel nanocrystals. This allowed us to precisely control the size of the magnetic nanocrystals and also the blocking temperature, T_b, of the system. Because blocking phenomena can mask the effects of exchange interaction, the T_b, must be lower than, or at least of similar order to, the inter-particle exchange coupling energy. The initial extent of exchange coupling in a GMF composite can be set by controlling the initial distance between nanocrystals. This is accomplished by utilizing the native surface ligands or adding bidentate ligands, such as oxalic acid and glutaric acid, to constrain particle distances. The second component of a GMF composite is the ferroelectric, which serves either as a matrix that the nanocrystals are mixed with, or as a substrate that the nanoparticles are deposited onto. In both cases, the ferroelectric is used to control the dielectric environment of the nanoparticles via an applied electric field, which in turn controls the magnetic state of the GMF composite. In general, the dielectric response of a ferroelectric material can be tuned in three ways. These include sweeping through the Curie temperature (T_C) of the ferroelectric using either (1) temperature or an (2) applied electric field, or (3) applying an electric field to cause domain

alignment in an unpoled ferroelectric that is well below its T_C. All three of these dielectric responses will be demonstrated in this work.

In order to separate the two dielectric responses, two ferroelectric materials were selected, specifically tetrathiafulvalene-p-chloranil (TTF-CA) [101] and potassium dihydrogen phosphate (KDP). TTF-CA is the archetypal organic ferroelectric with a 10-fold spike in the dielectric constant at the 81 K T_C phase transition for the paraelectric and ferroelectric phases [102]. This 10-fold dielectric increase at the phase transition occurs at an ideal temperature, where exchange coupling can be effectively influenced by changes in the dielectric environment. By sweeping through the T_C of the ferroelectric, the exchange coupling between nanocrystals embedded in a TTF-CA matrix should first increase and then decrease as the dielectric constant increases and decreases. This phase transition in TTF-CA can also be driven by an electric field if the system is slightly above the phase transition temperature. In contrast to TTF-CA which can show a dielectric response to both temperature and an electric field, KDP is a commercially available ferroelectric that has no phase changes in the temperature range relevant to this work. Unpoled KDP does show dielectric changes in response to an applied electric field due to domain alignment, a process which is independent of any phase transitions.

Using this combination of materials, we are able to reach all the requirements listed previously and provide the first experimental demonstration of an exchange coupled GMF composite. In the manuscript below, we first demonstrate the ability to control the inter-particle distances using diacid linkers and show that this control results in predictable changes in magnetic properties. We next demonstrate that exchange coupling in a GMF composite can be enhanced by adding a FE component into the system.. Finally, we investigate the electric field dependence of

both TTF-CA and KDP based GMF composites. In both cases, we demonstrate electric field control over magnetic properties that is dielectric mediated, and not based on traditional strain-mediated processes.

4.2. RESULTS AND DISCUSSION

4.2.1. Materials Characterization. The first step to building exchange coupled GMF composites is to fully characterize the magnetic nanocrystals and organic ferroelectric to ensure the parameters required for a GMF composite are met. Figure 4.2, shows characterization of Ni nanocrystals and TTF-CA used in this work. Solution processed methods were used to synthesize monodispersed Ni nanocrystals with diameters between 15-35 nm. Transmission electron microscopy (TEM) images (figure 2a) and X-ray diffraction (XRD) patterns (figure 4.2b) representative for samples used in this work confirm the size and crystallinity of the nanocrystals. These nanocrystals show reproducible magnetic properties with a blocking temperature (T_b) under ~150 K. By making smaller nanocrystals, we can tune the T_b to lower temperatures. The organic ferroelectric, TTF-CA, shows a reversible color change upon cooling to cryogenic temperatures (figure 4.2c), which is characteristic of the paraelectric to ferroelectric phase transition. The sample was further characterized using XRD (figure 4.2d) to confirm that the correct phase of TTF-CA was synthesized. In all cases, comparison of superconducting quantum interference device (SQuID) magnetometry measurements were carried out using the same batch of nanocrystals and ferroelectric to ensure that any differences between batches would not bias the results.

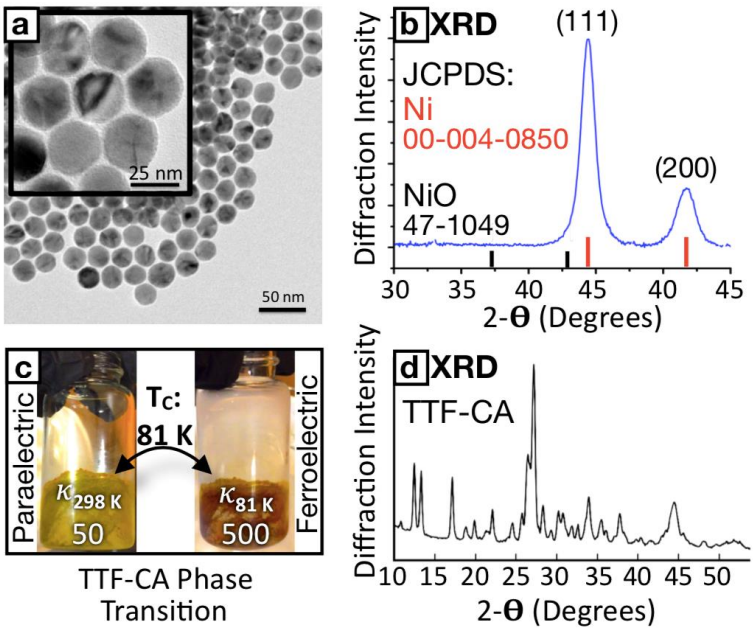

Figure 4.2: (a) TEM images of the monodispersed nickel nanocrystals used in this work. (b) Powder XRD of the Ni nanocrystals confirms that they have the correct crystal structure (red stick pattern) and that no crystalline NiO is present in the sample (black stick pattern). (c) The color change observed in our TTF-CA indicates a phase transition from the paraelectric phase at room temperature to the ferroelectric phase at liquid nitrogen temperatures. TTF-CA has an expected 81 K T_C and a 10-fold increase in dielectric constant near the transition. (d) Powder XRD of TTF-CA. Peak positions are in good agreement with literature values.

4.3.2. Temperature Dependent Magnetic Studies. Our next goal was to demonstrate that the inter-particle distance between nanocrystals could be controlled and that these changes would result in predictable changes in magnetic behavior based on the modified exchange coupling. The simplest experimental approach to vary the tunneling distance between nanocrystals is by modifying the surface ligands, exploiting bidentate ligands such as diacids, to precisely define the distance between nanocrystals based on molecular size. Appendix figure A1 shows TEM images

of a range of nanocrystals with different surface ligands used to control inter-particle distances. While it is hard to see the very small changes in the nanoparticle spacing due to focusing variations, from the TEM images it is clear that the diacids used have not significantly altered or etched the nanocrystal surface. SQuID magnetometry measurements of these samples (top panel, figure 4.3a) show a clear trend in the coercivity as a function of temperature between the different inter-particle distances. Sample M-H data used to plot coercivity as a function of temperature for the different inter-particle spacing, provided in the Appendix figure A2. Inter-particle interactions increase with decreasing inter-particle spacing, resulting in a monotonic increase in the coercivity of the ensemble at all temperatures for samples with smaller inter-particle distances. Samples shown in figure 4.3a, starting from the largest distances and going down, are: wax dispersed nanocrystals with a large spacing (a, black); nanoparticles linked using the 5 carbon diacid, glutaric acid (b, red); nanocrystals linked using the 2 carbon diacid, oxalic acid (c, green); and finally, aggregated nanocrystals that have been ligand stripped (d, blue). The monotonic increase in coercivity supports our hypothesis that controlling inter-particle distances between nanocrystals can be used to control inter-particle exchange coupling in GMF composites.

With the effect of inter-particle distance on nanocrystal magnetic properties established, the next step is to incorporate the ferroelectric material into the composite. The two ferroelectric materials used in this work were both selected for their tunable dielectric properties at low temperatures. In particular we studied TTF-CA and KDP. TTF-CA is the classic organic ferroelectric material, composed of electron donor and acceptor dimer chains, which undergo a neutral-to-ionic phase transition (space group $P2_1/n$ to Pn) at 81 K upon cooling [101]. Since the dielectric constant of the sample with the TTF-CA is much higher than that of the sample without TTF-CA the exchange coupling should increase due to the FE component according to the theoretical predictions in literature[41-44].

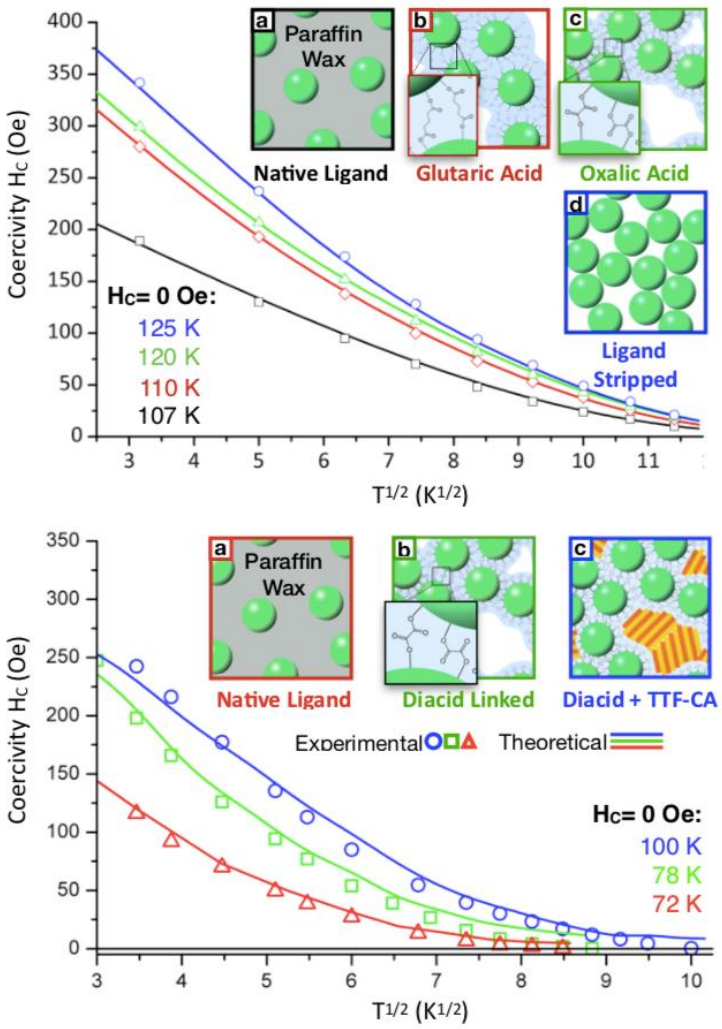

Figure 4.3: Top panel: SQuID magnetometry measurements of coercivity as a function of temperature. The data shows increasing coercivity with decreasing inter-particle distances due to increasing dipole-dipole and exchange couplings. Markers represent experimental data; solid lines are guides for the eyes. (a) nanoparticles in paraffin wax (black); (b) nanoparticles linked by glutaric acid (red); (c) nanoparticles linked by oxalic acid (green); and (d) aggregated, ligand stripped (blue). Bottom panel: SQuID magnetometry measurements of coercivity as a function of temperature for, (a) uncoupled wax dispersed nanocrystals (red); (b) exchange coupled oxalic acid linked nanocrystals (green); and (c) exchange coupled nanocrystals in a TTF-CA matrix, forming a GMF composite (blue). Markers indicate experimental data. Solid lines are derived from Monte-Carlo simulations of the experimental data.

To understand how the dielectric environment can change exchange coupling between nanoparticles, a series of three samples were made using a single batch of 15 nm monodispersed nanocrystals. This series included well-spaced nanocrystals made by dispersing as-synthesized ligand capped nanocrystals in a wax matrix, closely spaced nanocrystals linked with a short bidentate oxalic acid linker, and those same linked nanocrystals mixed with TTF-CA. The coercive field was then measured as a function of temperature for these samples, as shown in the bottom panel of figure 4.3. Markers represent experimental data, while the solid lines show the results of Monte Carlo simulations (see Appendix section for details of modeling). The as-synthesized nanocrystals dispersed in paraffin wax (a, red) serve as a control for a non-coupled system, which we model using only blocking phenomenon contributions— i.e. the coercive field depends only on the particle anisotropy and magnetic moment. The nanocrystals linked with oxalic acid (b, green) show an increased coercivity at all temperatures relative to the control. In this system, we expect that in addition to blocking contributions, the coercive field will also be influenced by both dipole-dipole interactions and exchange coupling contributions. Unfortunately, we cannot accurately differentiate between the changes in coercivity from dipole-dipole interactions and exchange coupling contributions, and so the diacid linked data (b, green) is fit using only blocking phenomenon contributions and dipole-dipole interactions. While we know that this assumption is not correct, and that some exchange coupling occurs in this sample, the exact fraction of each coupling component in the diacid linked sample is not particularly important for the conclusions of this work. The limiting assumption of only dipole-dipole coupling in the absence of a ferroelectric, lets us use this system as a baseline for the exchange coupling calculations described below. A more detailed explanation of how the dipole-dipole and exchange coupling interactions

are considered can be found in the Appendix section, under the subsection on modeling the temperature dependence of TTF-CA GMF composites.

When the exact same diacid linked nanocrystals are now incorporated into a TTF-CA matrix (c, blue), the resulting GMF composite shows both increased coercivity and an increased T_b. We thus assign both the 22 K increase in T_b and the fact that the coercive field is greater than that measured for the diacid linked sample without TTF-CA (b, green) at all temperatures, to the increased dielectric constant of the TTF-CA. This dielectric increase should enhance exchange coupling between the nanocrystals. For the TTF-CA containing sample (c, blue), the data is now fit by adding exchange coupling contributions to the parameters previously used to fit the diacid linked only sample (b, green). Generally, the ferroelectric should have a temperature dependent dielectric constant, ε, which would lead to a temperature dependent exchange interaction; however, we do not have independent data on the $\varepsilon(T)$ dependence and our modeling procedure can not uniquely define such a dependence. Therefore, we fit the experimental data assuming a temperature independent ε in the studied region. This is a reasonable assumption considering that our experimental samples are highly disordered and the ferroelectric phase transition could be smeared leading to a weak dependence of ε on T. This model gives a good fit to the experimental data. Thus, the increased exchange coupling our GMF samples is most likely related to the influence of dielectric properties on exchange coupling.

We note that we do not expect the observed change in magnetic anisotropy to be due in any part to the type of strain-mediated magnetoelectric effects that occur for rigid systems, such as epitaxial thin film on inorganic ferroelectric substrates [75, 77, 88]. TTF-CA, as an organic ferroelectric, is very soft [103] and should not be able to stretch or squeeze metallic nanocrystals,

which have a bulk Young's modulus of 220 GPa. For the Ni nanocrystal grain sizes used in this work, the Young's modulus is expected to be similar to the bulk value [104]. We also do not expect the ferroelectric to change the dipole-dipole coupling between nanocrystals because the average distance between the particles is governed by the diacid linker length and is thus fixed by the cross-linking. Therefore, the only likely effect from the TTF-CA is to tune the exchange coupling through changes in the dielectric environment.

4.3.3. Electric Field dependent Magnetic Properties. We next studied the influence of the electric field on Ni nanocrystal based GMF. This was done using two different ferroelectric materials, TTF-CA and KDP, using capacitor structures described in the Methods section. The dielectric constant of TTF-CA is sensitive to applied electric fields, particularly just above the T_C, where an applied electric field can be used to drive the system back through the paraelectric to ferroelectric phase transition. For samples at or just above the T_C, we thus expect a large increase in dielectric as a bias is applied, followed by a decrease in dielectric at higher field as the phase transition is complete. For lower temperature samples that are fully in the ferroelectric phase, dielectric changes are still expected upon application of a bias due to domain alignment, but the changes in the dielectric environment should be smaller. Here again, the dielectric constant is expected to first increase as the ferroelectric domains begin to polarize and then decrease as saturation is reached.

The coercivity as a function of applied voltage for a TTF-CA GMF composite is plotted in figure 4.4a. Markers show experimental data and solid lines are the results of Monte Carlo simulations. The composite GMF material was biased to a maximum of 400 V in a parallel plate capacitor setup with a total gap of roughly 500 μm. Measurements were taken very near the T_C of

TTF-CA, at 80 K, and well below the T_C, at 65 K. The average coercivity at 80 K is smaller than at 65 K, which is due to increased thermal fluctuations at the higher temperature. For both temperatures, there is a peak in coercivity around 80 V, but the magnitude of the change is much larger for the 80 K samples. According to our model, which describes how the dielectric constant of the ferroelectric changes with an applied electric field (see Eq. (2) in the Methods section), exchange coupling for the two temperatures should have a peak around the ferroelectric switching field. Assuming a 500 μm sample thickness, the switching field is estimated to be 1.6 kV/cm (approximately the same value for 65 K and 80 K), which is in reasonable agreement with the 5kV/cm switching field reported in literature for pure TTF-CA at 65 K.[101] The difference in values could be due to a number of factors, including uncertainty in our parallel plate capacitor sample thickness, the crystallinity of the TTF-CA, or due to the influence of grains and the complex system geometry. Regardless, the samples show a dramatic change in nanocrystal coercivity as the system is tuned through the TTF-CA curie transition using an electric field, indicating that exchange coupled GMF composites can indeed be realized in practical materials systems.

At 65 K, far from the T_C, the relative change in coercivity is fairly small (around 6% total variation of the coercive field). We assume that at this temperature, the dominant processes that can result in changes to the dielectric constant are domain reorientations, and so the dielectric changes should be modest. The fact that at 80 K, very near to the phase transition temperature, we see a much larger change in the coercivity (about 50% total variation of coercive field) is strong evidence that a different mechanism is active here. We conclude that at 80 K, in addition to domain reorientations, the electric field is also driving the neutral-to-ionic phase transition in TTF-CA, significantly enhancing the dielectric dependent exchange coupling interaction.

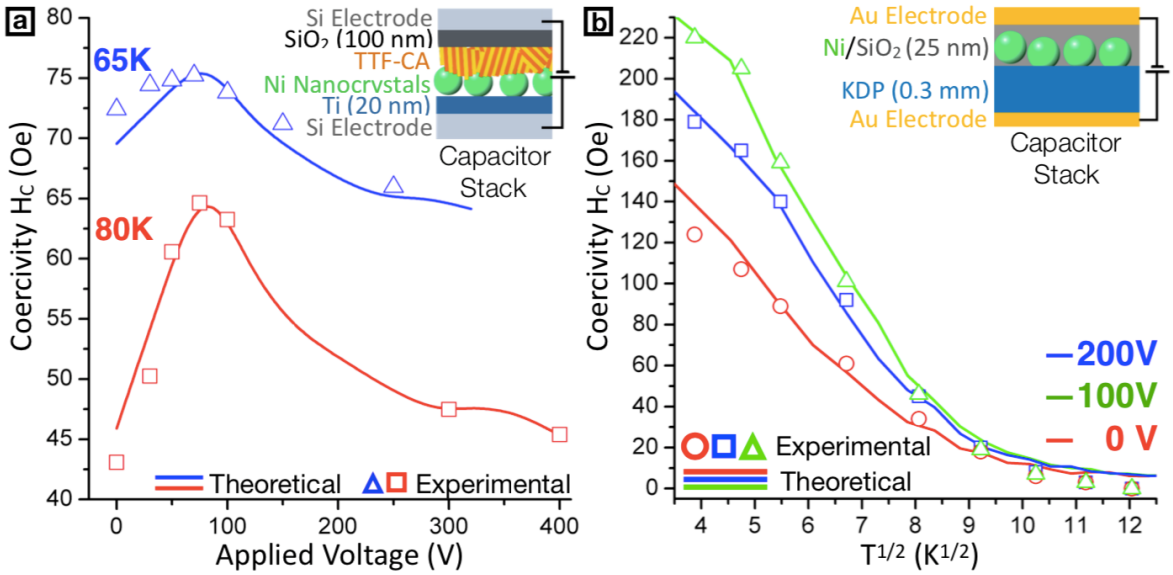

Figure 4.4. Electric field dependence for two different GMF composites. In both cases, the markers represent experimental data and the solid lines represent theoretical models. (a) Coercivity as a function of applied voltage is plotted for a TTF-CA GMF composite, with data obtained at 65 K and 80 K. The inset shows a cartoon schematic of the parallel plate capacitor setup used for biasing. At both temperatures, coercivity can be modified with a voltage and in both cases we observe, first an increase in the coercivity followed by a decrease, which is likely caused in part by ferroelectric domain reorientation. For the 80 K sample near the T_C of the TTF-CA, the magnitude of the change in coercivity is much larger, suggesting that the dielectric changes are enhanced by contributions from the paraelectric to ferroelectric phase transition. (b) Coercivity across the full temperature range for a KDP GMF composite at 0 V, 100 V, and 200 V. The inset shows a cartoon schematic of the parallel plate capacitor setup used for biasing the KDP GMF composite. Again, we observe that the coercivity first increases, when a moderate voltage of 100V is applied to the sample, and then decreases somewhat, when a larger voltage is applied. KDP should not have any phase transitions in this temperature range, so these changes are likely to be a purely domain alignment effect.

The experimental data is again fit using Monte Carlo simulations described in the Methods section and detailed in the Appendix section, in the subsection on modeling the voltage dependence of a TTF-CA GMF. The simulation results (solid lines) are generated using our dependence of the exchange interaction on electric field (Eq. (1) in the Methods section), combined with a simple model for the electric field dependence of the dielectric constant in the vicinity of the T_C (Eq. (2) in the Methods section). In general, the FE parameters (ε_0, $\Delta\varepsilon$, E_s, ΔE, and γ) as well as the electronic properties of the grains characterized by J_0, J_1, and α are dependent on temperature. The parameters that give the best fit are presented in the Appendix section. The modeling results are in excellent agreement with the experimental results (markers). Note that again in this case, strain-mediated magnetoelectric coupling should not be contributing to the observed data because of the very soft nature of the TTF-CA organic ferroelectric.

The 65 K data in figure 4.4a shows that some field dependent changes can be observed in the absence of a phase transition due to domain reorientation. We thus chose to further explore these effects in a GMF composite where there was no possibility of competing influences from phase transitions; and so, we repeated a similar voltage dependent experiment using the commercially available ferroelectric, KDP. KDP does not have any phase transitions in the temperature range of interest for exchange coupling. Thus, the voltage dependence of the coercivity for a KDP GMF composites can be investigated across the full temperature range where Ni shows a transition from ferromagnetic to superparamagnetic behavior. Specifically, in this set of experiments, a near monolayer of as-synthesized 15 nm monodispersed nanocrystals were spin coated onto a KDP wafer. The nanocrystals were then sputter coated with an insulating SiO_2 layer, followed by gold electrodes, as shown in the inset figure 4.4b. From previous work, we know that mechanical coupling between nanocrystals and a ferroelectric surface are inhibited by the organic

surface ligands on the nanocrystals,[17] and so we can disregard any strain-mediated magnetoelectric coupling in this sample.

Figure 4.4b shows the voltage dependence of a KDP GMF composite from 15 K to 145 K under a bias of 0 V (red), 100 V (green), and 200 V (blue). As before, the markers show experimental data and solid lines result from Monte Carlo modeling. In the model, we assume that the exchange interaction is independent of temperature, but strongly depends on the applied voltage, growing at moderate fields and decreasing at higher fields, as would be expected for domain alignment and saturation. One can see that the behavior of the coercive field as a function of voltage is similar to that observed for the TTF-CA GMF composite. The coercive field grows at low voltage, then decreases at high voltage as the system saturates, leading to what would be a peak in the coercive field as a function of voltage. The magnitude of the exchange coupling effect is quite large. At low temperature the coercive field increases almost 2-fold (increases 176% at 15 K) with an applied voltage. This large change at low temperature is in agreement with our model. More details of the simulations can be found in the Appendix section in the subsection on Modeling of KDP GMF composites.

Taken together, these results provide strong evidence that exchange coupled multiferroic composites can indeed be fabricated, and that the magnetic properties of the nanocrystals can be tuned using an applied electric field. Our work shows consistent observations using two fundamentally different ferroelectric materials. This is highly encouraging that this novel class of multiferroics could be generalized to a broader range of materials.

4.4. CONCLUSION

In the present work, we experimentally demonstrate a new type of multiferroic material, where a coupled nanocrystal array can be controlled by tuning the dielectric environment, which in turn effects the inter-particle exchange coupling interaction that governs the magnetic properties of the composite material. The composite material consists of an ensemble of metallic magnetic nanocrystals embedded in, or placed directly on top of, a ferroelectric matrix. We develop two GMF composites, using Ni nanocrystals integrated with the organic ferroelectric TTF-CA and Ni nanocrystals placed on top of the inorganic ferroelectric KDP. Using these materials, we demonstrated that one can tune the coercive field of the nanocrystals using an applied electric field. At low temperatures, the coercive field increases almost 2-fold with an applied electric field on the order of 3 kV/cm. We further performed Monte Carlo simulations to model the experimental data and showed that reasonable agreement between the experimental and theoretical results could be obtained. In the model, the mechanism of coupling depends on the interplay between Coulomb blockade effects, screening of Coulomb interactions, and exchange interactions in a granular material. This novel magnetoelectric coupling mechanism is unique to nanocrystal systems and cannot be observed in bulk or thin film composites. These multiferroic composite materials thus represents an entirely new class of multiferroics, unique in their coupling mechanism, but generalizable to any number of nanocrystal/ferroelectric designs.

4.5. METHODS

4.5.1 Synthesis of Ni nanocrystals. All reactions were carried out under an argon atmosphere using standard air-free techniques on a Schlenk line. Nickel (II) acetylacetonate (Aldrich, Tech., 90%), Oleylamine (Aldrich, 70%), trioctylphosphine (Aldrich, 97%), oleic acid

(alfa Aesar, Tech., 90%), and 1-octadecene (Acros Org., Tech., 90%) were all used without further purification.

The synthesis of nickel nanocrystals followed a modified version of the method developed by Carenco, S. et al.[29] The synthesis used standard air-free techniques on a Schlenk line under and argon atmosphere. Nickel nanocrystals were synthesized by the thermal decomposition of 1 mmol nickel acetylacetonate in the presence of ~18 mmol oleylamine (5.78 mL), 1 mmol oleic acid (0.315 mL), 2 mmol trioctylphosphine (0.91 mL), and sufficient 1-octadecene to fix the total volume at 7 mL. The solution was stirred while undergoing three pump/purge cycles over the course of 30 minutes at room temperature and then another three cycles at 90 ˚C, again over the course of 30 minutes, to remove trace oxygen/water from the precursors. The solution was then heated under inert atmosphere at 15 ˚C/min and refluxed at 220 ˚C for 45 minutes, followed by rapid cooling to room temperature after completion. The nanocrystals were then purified by adding 1 mL hexanes and 40 mL of ethanol to precipitate the nanocrystals. To improve monodispersity, a N52 neodymium magnet (25.4 mm diameter) was used to collect the nanocrystals in place of the standard centrifugation methods. Samples were then cleaned two addition times by resuspending the nanocrystals in 1 mL of hexane, reprecipitating with 40 mL ethanol, and collecting the powder by magnetic separation. The final solution was suspended in 20 mL of hexanes and used immediately. Nanocrystal sizes used for this work ranged from 15 nm to 35 nm in diameter, which could be tuned by varying the trioctylphosphine and oleylamine ratio.

4.5.2. Ferroelectric materials. Potassium dihydrogen phosphate substrates (4x4x0.3 mm, C-cut perpendicular to the 4x4 mm surface) were purchased from United Crystals Inc. and used as purchased. Bulk TTF-CA powder was synthesized using a modified version of the method described by Lapidus S. et al. [105]. Tetrathiafulvalene (TCI, 98%) and p-chloranil (Alfa Aesar, 97%)

were used without further purification. Generally, equimolar amounts of tetrathiafulvalene and p-chloranil were dissolved in toluene until saturated and then slowly dried under argon with mild mechanochemical mixing. The largest crystallites from the initial recrystallization were separated from any discolored or poorly crystalized sample. The samples were then recrystallized and sorted a second time to improve purity.

4.5.3. Controlling nanocrystal inter-particle distances. Here, we describe how the nanocrystal samples shown in the top panel of figure 4.3 were created. For the two diacid linked samples using oxalic and glutaric acid, small aliquots of as-synthesized nanocrystals were gently mixed with 10 mM solutions of the specific diacid dissolved in a 1:1 THF/hexane solvent, until the as-synthesized nanocrystals aggregated due to cross-linking. The now linked nanocrystals were then magnetically separated from the solution. The resulting powder was then washed three times in a solution of 1 ml of hexanes and 40 mL of ethanol, and recollected using a strong magnet, as described above. For consistency, both the wax dispersed and the aggregated samples followed identical processing methods as the diacid linked nanocrystals, except that their 1:1 THF/hexane solutions did not contain diacids.

To create the ligand stripped aggregated samples, a small aliquot of as-synthesized nanocrystals was sonicated in 20 mL of pure hexanes until the ligands had been removed by mass action. Precipitated nanocrystals could be removed with a strong magnet and would be further sonicated with pure hexanes until there were no longer any nanocrystals suspended in the supernatant. To make sure that sonication itself had no effect on the magnetic properties, all other samples were sonicated for the same total duration in their original solutions.

4.5.4. Granular multiferroic composite. The TTF-CA granular multiferroic (GMF) composite shown in the bottom panel of figure 4.3 was produced by mixing powders of TTF-CA crystals with diacid linked nanocrystals (1:10 Ni:TTF-CA ratio). The TTF-CA crystals in the mixture were then partially dissolved using small amounts of toluene and mild mechanical mixing to facilitate infiltration into the nanocrystal powder. The resulting slurry was then drop casted into a plastic pill capsule and measured by superconducting quantum interference device (SQuID) magnetometry as a powder.

The TTF-CA GMF composite for figure 4.4a used the previously discussed methods in Chapter 2 to adhere a monolayer of as-synthesized nickel nanocrystals to a titanium layer sputtered onto a doped silicon wafer. A slurry of TTF-CA crystals, again partly dissolved in toluene, was then drop casted onto the monolayer of nanocrystals and sandwiched between a second conductive silicon wafer to form a capacitor. Electrodes were bonded to the back of both conductive silicon wafers with conductive carbon tape.

The potassium dihydrogen phosphate (KDP) GMF composite, shown in figure 4.4b, was produced by spin coating a very thin (near monolayer) film of the as synthesized Ni nanocrystals directly onto the KDP wafer. The sample was then sputtered with 25 nm of SiO_2, followed by gold electrodes.

For all samples, only data from the same synthetic batch of nanocrystals and/or ferroelectric were compared to ensure consistency within a set of data. Due the nature of our materials, having both temperature and electric field dependent dielectric properties leading to rapidly changing dielectric constants, we reported only the applied bias for poled samples. In all

cases, when applied voltages are reported for a sample, the data is from a single sample so that relative changes can be accurately compared.

4.5.5. Magnetic and electrical measurements. Magnetization measurements were conducted using a Quantum Design MPMS superconducting quantum interference device (SQuID) based magnetometer using VSM mode. Electrical biasing was done in-situ using a Stanford Research System, Inc. power supply, model PS350/5000V-25W. Powder X-ray diffraction patterns (XRD) were measured using a PANalytical X'Pert Pro using a Cu Kα (λ = 1.5418 Å) source, operating at 45 kV and 40 mA. XRD patterns were recorded in the range of 30° < 2θ < 60°. Transmission electron microscope (TEM) images were taken using a FEI T12 Quick CryoEM system, operating at 300 kV.

4.5.6. Modeling of GMF composites. To understand the experimental data, we modeled the GMF using a Monte Carlo approach (see all details in the Appendix section). We took into account the uniaxial magnetic anisotropy of grains, as well as dipole-dipole interaction and exchange interactions between grains. We used different geometric arrangements of the grains in our simulations, which is shown to play an important role in dipole-dipole and exchange coupling interactions (see more details in the Appendix section). The magnetoelectric coupling effect was introduced into the model through the dependence of the inter-grain exchange coupling, $J(E)$, on electric field, E. Such a dependence appears due to the interplay of the Coulomb blockade and specific dependence of the ferroelectric dielectric constant on the electric field. The dependence of J on the dielectric constant, ε, is given by,

$$J(\varepsilon) = J_0 + J_1\left(1 - \sqrt{\alpha\varepsilon}\,\mathrm{atan}(1/\sqrt{\alpha\varepsilon})\right), \quad (1)$$

where α, J_0, and J_1 are defined by internal electronic structure of magnetic grains. In ferroelectric materials the dielectric constant strongly depends on electric field, growing with the applied electric field until it reaches a maximum at the ferroelectric polarization switching field. Further increasing the electric field leads to a reduction of the dielectric constant. We describe this behavior with the function,

$$\varepsilon(E) = \varepsilon_0 + \begin{cases} \frac{\Delta\varepsilon}{1+(|E-E_s|/\Delta E)^{\gamma_1}}, E < E_s, \\ \frac{\Delta\varepsilon}{1+(|E-E_s|/\Delta E)^{\gamma_2}}, E > E_s, \end{cases} \quad (2)$$

where, E_s is the ferroelectric switching field, ΔE is the peak width, $\gamma_{1,2}$ defines the behavior for the slope of the curve, ε_0 defines the dielectric constant at high field, and $\Delta\varepsilon$ is the variation of the dielectric constant. This function captures the main dependencies of the dielectric constant and allows us to fit the experimental data by varying the parameters in Eq. (2). Note, that all the parameters in the Eq. (2) are in general temperature dependent.

APPENDIX

Modeling of granular multiferroic composites: For this work, we described our system using the following Hamiltonian,

$$H = -\sum_i \lambda_i (\mathbf{m}_i \mathbf{n}_i)^2 + J(\varepsilon(E)) \sum_{<ij>} (\mathbf{m}_i \mathbf{m}_j) + \sum_{ij} M_i M_j \left(\frac{(\mathbf{m}_i \mathbf{m}_j)}{|\mathbf{r}_{ij}|^3} - \frac{3(\mathbf{m}_i \mathbf{r}_{ij})(\mathbf{m}_i \mathbf{r}_{ij})}{|\mathbf{r}_{ij}|^5} \right), \quad (1)$$

where $\mathbf{m}_i$ are the unit vectors co-directed with i particle magnetization and M_i is the particle magnetic moment. We used the uniaxial anisotropy constant, λ_i and randomly distributed the anisotropy axes, $\mathbf{n}_i$, over all possible directions. To mimic the nanocrystals used experimentally,

we took a log-normal size distribution of particles with the dispersion, σ_d. This size distribution provides a more realistic distribution of the anisotropy energies that are present in the experimental system. Interactions between nanocrystals are described by the inter-particle exchange coupling constant, J, using the vector, $\mathbf{r}_{ij}$, to describe connections between the particles i and j. J is dependent on dielectric constant of the ferroelectric matrix ε, which in turn depends on the external electric field, E. Brackets, <>, denote a summation over the nearest neighbors only. To study the Hamiltonian and our experimental results we used the Monte Carlo approach.

Here, we present the relevant assumptions used in our model. We note that according to the literature, the bulk Ni anisotropy constant depends on temperature [34]. However, the dependence is rather weak at lower temperatures (below 50 K) and so we neglect this phenomenon. We do not expect any Ni/NiO exchange bias effects to be present in our system based on our hysteresis loop measurements for this work and previous work investigating Ni/NiO nanocrystal exchange bias effects in Chapter 2. Therefore, our model does not take any exchange bias effects into account. We considered several different arrangements of particles: 1) randomly distributed particles far from neighboring particles (non-interacting); 2) a close-packed system; 3) randomly distributed and oriented chains of particles. The number of particles modeled in the ensemble varied from 50 to 300 for this work.

The dependence of the exchange interaction, J, on electric field: According to recent theoretical predictions, the exchange interaction between two magnetic particles depends in part on the dielectric constant of the ferroelectric matrix and therefore on the electric field applied to the system. Following Ref.[41], we used the equation Eq. (1), from the Methods section, to describe

the exchange coupling, where α is defined by internal electronic structure of magnetic grains. Using Eq. (1) we fit our experimental data by varying the parameters J_0, J_1, and α.

The most important contribution from our model is describing this exchange coupling interaction, J, and how it depends on the dielectric constant of the ferroelectric matrix. This dependence represents the novel magnetoelectric coupling, which is the fundamental goal driving the bottom-up design for our nanocrystal-based GMF composite.

The dependence of the dielectric constant, ε, on electric field: In our simulations we assumed that the dielectric constant depends on the applied electric field. In general, the dielectric constant grows with the electric field until it saturates at the ferroelectric polarization switching field. Increasing the electric field further reduces the dielectric constant. We describe this behavior with Eq. (2), in the Methods section, where E_s is the ferroelectric switching field, ΔE is the peak width, $\gamma_{1,2}$ defines the behavior for the slope of the curve, ε_0 defines the dielectric constant at high field, and $\Delta\varepsilon$ is the variation of the dielectric constant. This function captures the main dependencies of the dielectric constant and allows us to fit the experimental data by varying the parameters in Eq. (2).

Monte Carlo modeling procedure: We followed a standard approach in which at each Monte Carlo step we randomly chose a magnetic particle and randomly rotated its magnetic moment. The maximum deviation of magnetic moment is chosen to obtain a high enough acceptance rate, where the acceptance probability is 1 if the energy of the new system state is less than the energy of old state. The acceptance probability is described as $\sim e^{-\Delta E/k_B T}$, if the energy difference between the new and old state ΔE is positive. Using this Monte Carlo approach, we calculated the coercive field dependence of the system with respect to the temperature, T.

We must also account for the simultaneous effects of dipole-dipole and exchange interaction between the particles. The dipole-dipole interaction was treated as finite for all pairs of particles and we used both open and periodic open boundary conditions for dipole-dipole interactions. In general, the results were qualitatively similar for both boundary conditions types. For the exchange interaction, we treated it as non-zero only for nearest neighbors and assumed the exchange coupling was the same for all interacting pairs of grains.

Modeling of a TTF-CA based GMF. Temperature dependence: This section describes the general model used to fit experimental data for nanocrystals that are considered non-interacting, i.e. native ligand samples that are dispersed in paraffin wax. The coercive field for these non-interacting samples depends only on the particle anisotropy and magnetic moment. As a specific example, the solid red line in the bottom graph in figure 4.3 represents the theoretical fit for non-interacting particles using our Monte Carlo simulations. For clarity, we will detail all of the relevant parameters for this specific simulation. We set the magnetization to be the same as the bulk Ni value, $M_s = 450$ Gs. We assume that the anisotropy axes are randomly distributed among all possible directions. We set the value for the average anisotropy constant $\lambda = 1.6 \cdot 10^5$ erg/cm^3. Note, this value is rather close to the data obtained in other experiments with Ni particles [83, 106]. One can see that the behavior of the $H_c(T)$ does not plot a straight line, which would be expected based on the well-known Neel-Brown law $\sim 1 - \sqrt{T/T_b}$ [107-109]. The curvature in our fit reflects the distribution of particle sizes in our synthesized nanocrystals. The best fit is obtained when the relative particle dispersion is about 0.6.

Next, we detail the general model used to fit closely-spaced nanocrystals, referred to as diacid linked in the experiment, which have aspects of both exchange coupling and dipole-dipole

coupling. As an example, the coercive field $H_c(T)$ for such fits can be seen in the bottom graph of figure 4.3, by the solid green line. The inter-particle distance for diacid linked samples is assumed to be on the order 0.5 nm. Therefore, the inter-particle distance is estimated as 1 nm. With such small inter-particle distances and high packing densities, the dipole-dipole interactions and exchange coupling interactions will both strongly influence the coercive field of the system. To fit this data set, we used the previous parameters obtained from the non-interacting sample model to set the magnetic anisotropy constant and the magnetic moment.

We will address the influence of dipole-dipole interaction for this diacid linked system. Because we cannot separate the effects of dipole-dipole interactions and exchange coupling interactions experimentally, we err on the conservative side and first attempt to explain our diacid linked system only with dipole-dipole interactions. There is a vast literature on the influence of dipole-dipole interactions on the magnetic properties of granular systems [110-115]. For dilute samples, dipole-dipole interactions typically behave as one would expect, causing only a slight increase in the coercive field [116, 117]. However, for high density 3D particle geometries, such as our diacid linked samples, the dipole-dipole interactions are expected to produce a decrease in the coercive field [111]. As one can see in the bottom graph of figure 4.3, the coercive field for our diacid linked sample (green squares) is in opposition to this statement, having a higher H_C, across all temperatures compared to the non-interacting sample (red triangles). In some cases, modeling shows that the dipole-dipole interaction for densely packed systems can indeed increase the coercive field, but this is only at high temperature [107]. It would be tempting to explain this enhanced coercive field simply due to exchange coupling interactions, however we first explored two other approaches to potentially explain this increased H_C. At first, we introduced ferromagnetic exchange coupling into our model. It is well known that such a coupling increases the coercive

field and might explain our data [118, 119]. While one can produce an increased H_c with ferromagnetic exchange coupling, the whole curve cannot be fitted using this approach. The second approach seeks to mimic the disorder found in experimental systems by varying the geometric configurations of the magnetic particles. From the TEM images shown in the Appendix, figure A1, the sample geometry is both chaotic and ordered in very complex configurations, potentially having chains of particles and even needles like structures in the sample. In a chain the dipole-dipole interactions would align all magnetic moments along the chain in head to tail manner. The dipole-dipole interactions of such chains could increase the coercive field based on literature [120]. Thus, we modeled our system as a number of chains (non-interacting) randomly oriented and distributed in space. The magnetic anisotropy of each particle is randomly oriented and independent of chain position and direction. We tried different length of magnetic chains from about 3 to 15 particles. Our Monte Carlo simulations show that using this chained geometry, dipole-dipole interactions alone can lead to an enhanced coercive field across the whole temperature range of interest. However, even with this complex geometry, our model produced a poor fit using solely dipole-dipole interactions. In order to obtain the best fit with a reasonable chain length configuration, we required both dipole-dipole coupling and exchange coupling interactions to be modeled. The best fit is shown by the solid green curve in the bottom graph of figure 4.3. With this model, we have developed a more realistic sample geometry, consisting of particle chains, and shown evidence for exchange interactions between our particles.

Because our modeling is based on geometry, there are in fact multiple configurations of chain lengths and widths that could yield similar best fits of the experimental. We limited our survey of chain configurations to 1x2xL ribbon chains and 2x2xL rectangular prism chains, where the chain length, L is varied in our model. For example, a ribbon chain of length L also gives good

agreement with the experimental data, when L is about 15 particles. This is quite reasonable based on our work with TEM characterization of nanocrystal clusters. In general, the magneto-dipole interaction induced anisotropy depends on the chain form factor. If one makes the chain thicker one has to make it longer. There are however, important differences between the chains with different lateral sizes, since the average number of nearest neighbors grows with lateral size. In a chain 1x1xL most of the particles have 2 neighbors, while in the 2x1xL ribbon there are three nearest neighbors for most particles. This is quite important when we consider the behavior of exchange coupling, which directly depends on the interactions with nearest neighbors. It is well-known that the effective Weiss field (the effective field produced by the inter-particle exchange) linearly depends on the number of nearest neighbors. In a linear chain (1 by 1 transversal size) the Weiss field is weaker than in a ribbon (1 by 2 transversal size) at the same exchange coupling constant J. In a ribbon, the field is weaker when compared to a rectangular prism chain (2 by 2 transversal size) and etc. The transversal size of clusters in the real sample can be significantly larger. Therefore, the effective Weiss field is bigger. In our model we increase the two-particle exchange interaction to model large transversal size of clusters.

Finally, we discuss the methods for the model for the GMF sample, which consists of a ferroelectric added to the magnetic chains, shown by the solid blue line in the bottom graph of figure 4.3. In our model, we assume the ferroelectric does not change the magnetic anisotropy of individual particles. Because the organic ferroelectric used in the experiment is soft, it is unlikely to stretch or squeeze magnetic particles. We also assume the ferroelectric does not alter the distance between the particles. One can see that adding the ferroelectric increases the coercive field at higher temperatures. To explain the increase in the coercive field we assume that the TTF-CA influences the exchange interaction between particles. The detailed mechanism of such an

influence is considered in Refs. [41-45]. In general, the ferroelectric matrix tunes the average dielectric environment surrounding the nanocrystals, leading to variation in the exchange coupling. We fit the data using the anisotropy, magnetization, and particle arrangement obtained in previous experiments and only tuned the exchange coupling for this GMF sample, solid blue line, bottom graph figure 4.3. We found that the exchange interaction increased to 600 K for this system with ferroelectric matrix, compared to 100K for the previously discussed diacid linked sample. Probably this value is grossly overestimated, since we expect real systems to potentially have massive chains and higher coordination number (number of nearest neighbors). In our chain model (1x1xL) only the neighboring particles interact, so the coordination number is 2. Moreover, the chains do not interact with other chains. In the real system, the chains may interact with each other and instead of chains, the particles may form agglomerates with unique shape anisotropy and higher average coordination numbers.

Modeling of a TTF-CA based GMF. Voltage dependence: We fit the experimental data in figure 4.4a using Monte Carlo simulations. To fit the data, we assumed that the exchange interaction depends on the applied electric field according to Eqs. (1) and (2). In the modeling we used the same anisotropy constant, particle size, and size distribution as in the previous section. We also modeled the system as an ensemble of particle chains. Good agreement can be obtained with different types of chains, for example 2x1x15 ribbons and 1x1x3 chains have similar agreement. However, the fitting parameters in the latter case are not very realistic. In particular, the exchange interaction should be of order of 5000 K for 1x1x3 chains. This is related to the fact that exchange interaction has only a minor effect in linear chains, where the average number of nearest neighbors is less than 2. A real system would be expected to have a much higher coordination number. With a higher coordination number, the effect of the exchange coupling

becomes more pronounced and the magnitude of the exchange coupling becomes much more reasonable.

Here we detail the list of relevant parameters used to produce the fit for figure 4.4a. Chain dimensions are 2x1x15, $\varepsilon_0 = 10$, $\Delta\varepsilon = 50$ (for 80 K) and $\Delta\varepsilon = 20$ (for 65 K), $\gamma_1 = 2.5, \gamma_2 = 0.8$, $V_s = E_s d$=80 V, $\Delta E = 50$ V, $J_1 = 1300$ K (for 80 K) and $J_1 = 900$ K (for 65 K), $\alpha = 0.15$. Note that the voltage dependence of the dielectric constant is different for different temperatures. This is because in the vicinity of the ferroelectric phase transition, $T = 80$ K, the dielectric constant is significantly more sensitive to an applied electric field. This gives a higher variation of the exchange coupling and finally the coercive field. We also note that the obtained value of the dielectric constant is much smaller than experimental data for TTF-CA from other papers [101]. This is due to two factors. First, in Eq. (2) the effective dielectric constant is used, which is the average dielectric constant of the whole mixture of grains and ferroelectric. This effective dielectric constant should be smaller than that of pure ferroelectric. Second, the dielectric constant of TTF-CA could be much smaller in our samples simply due to defects or impurities during synthesis. The complicated geometry of the sample most likely also contributes to the lowered average dielectric constant.

Modeling of a KDP GMF: We assumed that the influence of the electric field tunes the dielectric constant of the ferroelectric. It is also assumed that the dielectric constant is independent of temperature and therefore the exchange interaction is also temperature-independent. Three Monte Carlo curves in figure 4.4b are plotted for the same system parameters excluding the exchange coupling. We used the similar parameters as in previous experiments and similar particle arrangements.

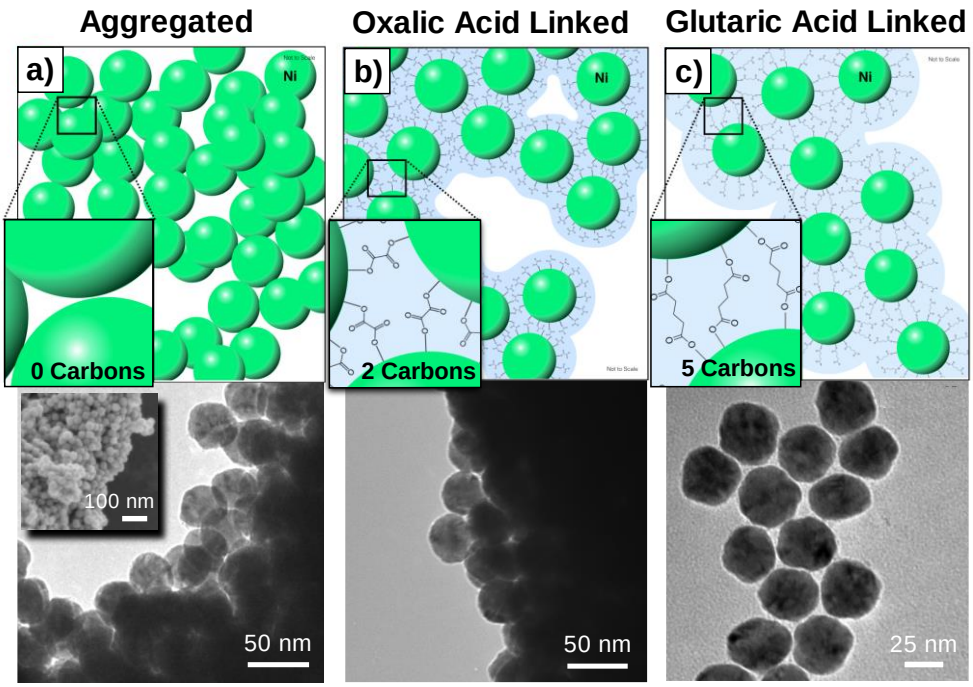

Appendix figure A1: Cartoon schematic and microscopy images of diacid linked Ni nanocrystals. (a) 0 carbon, aggregated nanocrystals without diacid linkers. (Inset) SEM of aggregated nanocrystals (b) 2 carbon, oxalic acid linked Ni nanocrystals. (c) 5 carbon, glutaric acid linked Ni nanocrystals.

Transmission electron microscopy images of diacid linked nanocrystals: Cartoon schematics of nanocrystals with varied inter-particle distances. TEM images of nanocrystals that have modified surfaces to control inter-particle distances. From the TEM images it is clear that the diacids used have not significantly altered or etched the nanocrystal surface. There is a well-defined inter-particle spacing for glutaric acid, however due to aggregation, we were not fortunate enough to characterize the spacing for other samples.

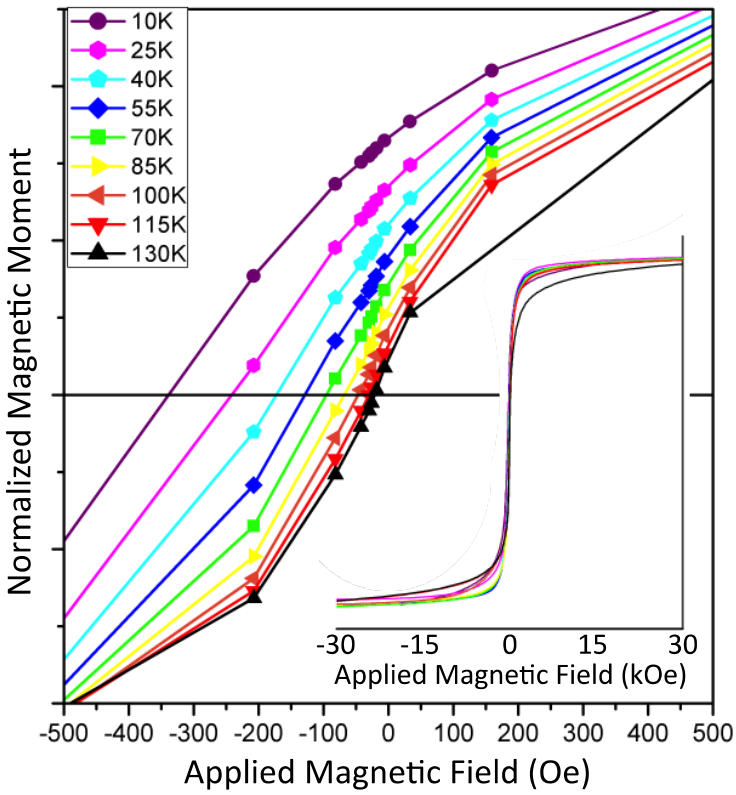

Appendix figure A2: M-H curves across a range of temperatures for ligand stripped nanocrystal sample used in the top panel figure 3. Shape markers represent experimental data and solid lines are provided as a guide for the eyes. Inset provides the full range of the applied magnetic field. Increasing coercivity is observed as a function of decreasing temperature.

M-H curves for ligand stripped nanocrystals: Magnetic as a function of applied magnetic field (M-H) loops were collected via SQuID magnetometry using VSM mode. A maximum 30 kOe applied magnetic field was used. To reduce measurement time, half M-H loops were taken after establishing that this did not alter the collected data. The half loops were fitted using a non-linear BiDoseRep function in Origin Pro. Typically fits were rejected if adjusted R-squared value is below 0.999. Coercivity ($H_C = 0$) was defined as the horizontal intercept of the half M-H hysteresis loop fit. Some data points are manually removed due improper fitting from

the built-in MPMS SQuID magnetometer software. This is the general method used to develop all coercivity plots presented in this work.

BIBLIOGRAPHY:

1. Park, J.; Lee, E.; Hwang, N. M.; Kang, M.; Kim, S. C.; Hwang, Y.; Park, J. G.; Noh, H. J.; Kim, J. Y.; Park, J. H., One-nanometer-scale size-controlled synthesis of monodisperse magnetic Iron oxide nanoparticles. *Angewandte Chemie* **2005,** *117* (19), 2932-2937.
2. Xia, Y.; Xiong, Y.; Lim, B.; Skrabalak, S. E., Shape-controlled synthesis of metal nanocrystals: simple chemistry meets complex physics? *Angewandte Chemie International Edition* **2009,** *48* (1), 60-103.
3. Hou, Y.; Kondoh, H.; Ohta, T., Size-controlled synthesis and magnetic studies of monodisperse FePd nanoparticles. *Journal of nanoscience and nanotechnology* **2009,** *9* (1), 202-208.
4. Park, T.-J.; Papaefthymiou, G. C.; Viescas, A. J.; Moodenbaugh, A. R.; Wong, S. S., Size-dependent magnetic properties of single-crystalline multiferroic BiFeO3 nanoparticles. *Nano letters* **2007,** *7* (3), 766-772.
5. Trunova, A. V.; Meckenstock, R.; Barsukov, I.; Hassel, C.; Margeat, O.; Spasova, M.; Lindner, J.; Farle, M., Magnetic characterization of iron nanocubes. *Journal of Applied Physics* **2008,** *104* (9), 093904.
6. Chen, W.; Wang, Z. H.; Ke, C.; Zhu, W.; Tan, O. K., Preparation and characterization of Pb(Zr0.53Ti0.47)O3/CoFe2O4 composite thick films by hybrid sol–gel processing. *Materials Science and Engineering: B* **2009,** *162* (1), 47-52.
7. Pan, Y.; Jia, R.; Zhao, J.; Liang, J.; Liu, Y.; Liu, C., Size-controlled synthesis of monodisperse nickel nanoparticles and investigation of their magnetic and catalytic properties. *Applied Surface Science* **2014,** *316*, 276-285.

8. Åkerman, J., Toward a universal memory. *Science* **2005,** *308* (5721), 508-510.

9. Kent, A. D.; Worledge, D. C., A new spin on magnetic memories. *Nature nanotechnology* **2015,** *10* (3), 187.

10. Wang, K. L.; Lee, H.; Amiri, P. K., Magnetoelectric random access memory-based circuit design by using voltage-controlled magnetic anisotropy in magnetic tunnel junctions. *IEEE Transactions on Nanotechnology* **2015,** *14* (6), 992-997.

11. Brataas, A.; Kent, A. D.; Ohno, H., Current-induced torques in magnetic materials. *Nature materials* **2012,** *11* (5), 372.

12. Hu, J.-M.; Li, Z.; Chen, L.-Q.; Nan, C.-W., High-density magnetoresistive random access memory operating at ultralow voltage at room temperature. *Nature communications* **2011,** *2*, 553.

13. Zhao, Z.; Jamali, M.; D'Souza, N.; Zhang, D.; Bandyopadhyay, S.; Atulasimha, J.; Wang, J.-P., Giant voltage manipulation of MgO-based magnetic tunnel junctions via localized anisotropic strain: A potential pathway to ultra-energy-efficient memory technology. *Applied Physics Letters* **2016,** *109* (9), 092403.

14. Hu, J.-M.; Li, Z.; Wang, J.; Nan, C., Electric-field control of strain-mediated magnetoelectric random access memory. *Journal of Applied Physics* **2010,** *107* (9), 093912.

15. Barangi, M.; Erementchouk, M.; Mazumder, P., Towards developing a compact model for magnetization switching in straintronics magnetic random access memory devices. *Journal of Applied Physics* **2016,** *120* (7), 073901.

16. Spaldin, N. A., *Magnetic materials: fundamentals and applications*. Cambridge University Press: 2010.

17. Kim, H. K.; Schelhas, L. T.; Keller, S.; Hockel, J. L.; Tolbert, S. H.; Carman, G. P., Magnetoelectric control of superparamagnetism. *Nano letters* **2013,** *13* (3), 884-888.

18. Chandra, S.; Huls, N. F.; Phan, M.; Srinath, S.; Garcia, M.; Lee, Y.; Wang, C.; Sun, S.; Iglesias, O.; Srikanth, H., Exchange bias effect in Au-Fe3O4 nanocomposites. *Nanotechnology* **2014,** *25* (5), 055702.

19. Mourdikoudis, S.; Liz-Marzan, L. M., Oleylamine in nanoparticle synthesis. *Chemistry of Materials* **2013,** *25* (9), 1465-1476.

20. Carenco, S.; Labouille, S.; Bouchonnet, S.; Boissière, C.; Le Goff, X. F.; Sanchez, C.; Mezailles, N., Revisiting the molecular roots of a ubiquitously successful synthesis: Nickel (0) nanoparticles by reduction of [Ni (acetylacetonate) 2]. *Chemistry–A European Journal* **2012,** *18* (44), 14165-14173.

21. Boles, M. A.; Ling, D.; Hyeon, T.; Talapin, D. V., The surface science of nanocrystals. *Nature materials* **2016,** *15* (2), 141.

22. Taniyama, T., Electric-field control of magnetism via strain transfer across ferromagnetic/ferroelectric interfaces. *Journal of Physics: Condensed Matter* **2015,** *27* (50), 504001.

23. Cherifi, R.; Ivanovskaya, V.; Phillips, L.; Zobelli, A.; Infante, I.; Jacquet, E.; Garcia, V.; Fusil, S.; Briddon, P.; Guiblin, N., Electric-field control of magnetic order above room temperature. *Nature materials* **2014,** *13* (4), 345.

24. Rosen, E. L.; Buonsanti, R.; Llordes, A.; Sawvel, A. M.; Milliron, D. J.; Helms, B. A., Exceptionally mild reactive stripping of native ligands from nanocrystal surfaces by using Meerwein's salt. *Angewandte Chemie International Edition* **2012,** *51* (3), 684-689.

25. Kim, J.; Rong, C.; Liu, J.; Sun, S., Dispersible Ferromagnetic FePt Nanoparticles. *Advanced Materials* **2009,** *21* (8), 906-906.

26. Gehl, B.; Frömsdorf, A.; Aleksandrovic, V.; Schmidt, T.; Pretorius, A.; Flege, J. I.; Bernstorff, S.; Rosenauer, A.; Falta, J.; Weller, H., Structural and Chemical Effects of Plasma Treatment on Close-Packed Colloidal Nanoparticle Layers. *Advanced Functional Materials* **2008,** *18* (16), 2398-2410.

27. Nadeem, K.; Ullah, A.; Mushtaq, M.; Kamran, M.; Hussain, S.; Mumtaz, M., Effect of air annealing on structural and magnetic properties of Ni/NiO nanoparticles. *Journal of Magnetism and Magnetic Materials* **2016,** *417*, 6-10.

28. Li, D.; Poudyal, N.; Nandwana, V.; Jin, Z.; Elkins, K.; Liu, J. P., Hard magnetic FePt nanoparticles by salt-matrix annealing. *Journal of applied physics* **2006,** *99* (8), 08E911.

29. Carenco, S.; Boissiere, C.; Nicole, L.; Sanchez, C.; Le Floch, P.; Mézailles, N., Controlled design of size-tunable monodisperse nickel nanoparticles. *Chemistry of Materials* **2010,** *22* (4), 1340-1349.

30. Taylor, S.; Zhang, J.; Eccleston, W., A review of the plasma oxidation of silicon and its applications. *Semiconductor science and technology* **1993,** *8* (7), 1426.

31. Jun, J.; Shin, J.-H.; Dhayal, M., Surface state of TiO2 treated with low ion energy plasma. *Applied surface science* **2006,** *252* (10), 3871-3877.

32. Sasi, B.; Gopchandran, K., Nanostructured mesoporous nickel oxide thin films. *Nanotechnology* **2007,** *18* (11), 115613.

33. Huang, W.; Zhu, J.; Zeng, H.; Wei, X.; Zhang, Y.; Li, Y., Strain induced magnetic anisotropy in highly epitaxial Co Fe 2 O 4 thin films. *Applied physics letters* **2006,** *89* (26), 262506.

34. Johnston-Peck, A. C.; Wang, J.; Tracy, J. B., Synthesis and structural and magnetic characterization of Ni (Core)/NiO (Shell) nanoparticles. *ACS nano* **2009,** *3* (5), 1077-1084.

35. Nan, C.-W.; Bichurin, M. I.; Dong, S.; Viehland, D.; Srinivasan, G., Multiferroic magnetoelectric composites: Historical perspective, status, and future directions. *Journal of Applied Physics* **2008,** *103* (3), 031101.

36. Song, C.; Cui, B.; Li, F.; Zhou, X.; Pan, F., Recent progress in voltage control of magnetism: Materials, mechanisms, and performance. *Progress in Materials Science* **2017,** *87*, 33-82.

37. Cheong, S.-W.; Mostovoy, M., Multiferroics: a magnetic twist for ferroelectricity. *Nature materials* **2007,** *6* (1), 13.

38. Hou, H.; Finkel, P.; Staruch, M.; Cui, J.; Takeuchi, I., Ultra-low-field magneto-elastocaloric cooling in a multiferroic composite device. *Nature Communications* **2018,** *9* (1), 4075.

39. Shankar, S.; Kumar, M.; Tuli, V.; Thakur, O. P.; Jayasimhadri, M., Energy storage and magnetoelectric coupling in ferroelectric–ferrite composites. *Journal of Materials Science: Materials in Electronics* **2018,** *29* (21), 18352-18357.

40. Chung Ming, L.; Jiefang, L.; Viehland, D.; Zhuang, X., A review on applications of magnetoelectric composites: from heterostructural uncooled magnetic sensors, energy harvesters to highly efficient power converters. *Journal of Physics D: Applied Physics* **2018,** *51* (26), 263002.

41. Udalov, O.; Beloborodov, I., Influence of the Coulomb interaction on the exchange coupling in granular magnets. *Journal of Physics: Condensed Matter* **2017,** *29* (15), 155801.

42. Udalov, O. G.; Beloborodov, I. S., Competition of the Coulomb and hopping-based exchange interactions in granular magnets. *Physical Review B* **2017,** *95* (4), 045427.

43. Udalov, O.; Chtchelkatchev, N.; Beloborodov, I., Phenomenological theory of magnetoelectric coupling in granular multiferroics. *Physical Review B* **2015,** *92* (4), 045406.

44. Udalov, O.; Chtchelkatchev, N.; Beloborodov, I., Electric field control of magnetic properties and magneto-transport in composite multiferroics. *Journal of Physics: Condensed Matter* **2015,** *27* (18), 186001.

45. Udalov, O. G.; Chtchelkatchev, N. M.; Beloborodov, I. S., Coupling of ferroelectricity and ferromagnetism through Coulomb blockade in composite multiferroics. *Physical Review B* **2014,** *89* (17), 174203.

46. Ma, J.; Hu, J.; Li, Z.; Nan, C.-W., Recent Progress in Multiferroic Magnetoelectric Composites: from Bulk to Thin Films. *Advanced Materials* **2011,** *23* (9), 1062-1087.

47. Yang, J. J.; Zhao, Y. G.; Tian, H. F.; Luo, L. B.; Zhang, H. Y.; He, Y. J.; Luo, H. S., Electric field manipulation of magnetization at room temperature in multiferroic

CoFe2O4/Pb(Mg1/3Nb2/3)0.7Ti0.3O3 heterostructures. *Applied Physics Letters* **2009,** *94* (21), 212504.

48. Thiele, C.; Dörr, K.; Bilani, O.; Rödel, J.; Schultz, L., Influence of strain on the magnetization and magnetoelectric effect in La0.7A0.3MnO3/PMN-PT(001) (A=Sr,Ca). *Physical Review B* **2007,** *75* (5), 054408.

49. Sahoo, S.; Polisetty, S.; Duan, C.-G.; Jaswal, S. S.; Tsymbal, E. Y.; Binek, C. J. P. R. B., Ferroelectric control of magnetism in Ba Ti O 3⁄Fe heterostructures via interface strain coupling. **2007,** *76* (9), 092108.

50. Hu, J.-M.; Nan, C.-W.; Chen, L.-Q., Size-dependent electric voltage controlled magnetic anisotropy in multiferroic heterostructures: Interface-charge and strain comediated magnetoelectric coupling. *Physical Review B* **2011,** *83* (13), 134408.

51. Tomoyasu, T., Electric-field control of magnetism via strain transfer across ferromagnetic/ferroelectric interfaces. *Journal of Physics: Condensed Matter* **2015,** *27* (50), 504001.

52. Cheng-Yen, L.; Scott, M. K.; Abdon, E. S.; Alexandre, B.; Wei-Yang, S.; Kyle, W.; Gregory, P. C., Modeling of magnetoelastic nanostructures with a fully coupled mechanical-micromagnetic model. *Nanotechnology* **2014,** *25* (43), 435701.

53. Liang, C.-Y.; Keller, S. M.; Sepulveda, A. E.; Sun, W.-Y.; Cui, J.; Lynch, C. S.; Carman, G. P., Electrical control of a single magnetoelastic domain structure on a clamped piezoelectric thin film—analysis. *Journal of Applied Physics* **2014,** *116* (12), 123909.

54. Peng, R.-C.; Hu, J.-M.; Momeni, K.; Wang, J.-J.; Chen, L.-Q.; Nan, C.-W., Fast 180° magnetization switching in a strain-mediated multiferroic heterostructure driven by a voltage. *Scientific Reports* **2016,** *6*, 27561.

55. Wang, Q.; Li, X.; Liang, C.-Y.; Barra, A.; Domann, J.; Lynch, C.; Sepulveda, A.; Carman, G., Strain-mediated 180° switching in CoFeB and Terfenol-D nanodots with perpendicular magnetic anisotropy. *Applied Physics Letters* **2017,** *110* (10), 102903.

56. Andres, C. C.; Anthony, B.; Gregory, P. C., Voltage control of magnetic monopoles in artificial spin ice. *Journal of Physics D: Applied Physics* **2018,** *51* (23), 234001.

57. Cui, J.; Liang, C.-Y.; Paisley, E. A.; Sepulveda, A.; Ihlefeld, J. F.; Carman, G. P.; Lynch, C. S., Generation of localized strain in a thin film piezoelectric to control individual magnetoelectric heterostructures. *Applied Physics Letters* **2015,** *107* (9), 092903.

58. Cui, J.; Hockel, J. L.; Nordeen, P. K.; Pisani, D. M.; Liang, C.-y.; Carman, G. P.; Lynch, C. S., A method to control magnetism in individual strain-mediated magnetoelectric islands. *Applied Physics Letters* **2013,** *103* (23), 232905.

59. Sohn, H.; Nowakowski, M. E.; Liang, C.-y.; Hockel, J. L.; Wetzlar, K.; Keller, S.; McLellan, B. M.; Marcus, M. A.; Doran, A.; Young, A.; Kläui, M.; Carman, G. P.; Bokor, J.; Candler, R. N., Electrically Driven Magnetic Domain Wall Rotation in Multiferroic Heterostructures to Manipulate Suspended On-Chip Magnetic Particles. *ACS Nano* **2015,** *9* (5), 4814-4826.

60. Gilbert, I.; Chavez, A. C.; Pierce, D. T.; Unguris, J.; Sun, W.-Y.; Liang, C.-Y.; Carman, G. P., Magnetic microscopy and simulation of strain-mediated control of magnetization in PMN-PT/Ni nanostructures. *Applied Physics Letters* **2016,** *109* (16), 162404.

61. Balinskiy, M.; Chavez, A. C.; Barra, A.; Chiang, H.; Carman, G. P.; Khitun, A., Magnetoelectric Spin Wave Modulator Based On Synthetic Multiferroic Structure. *Scientific Reports* **2018,** *8* (1), 10867.

62. Chavez, A. C.; Sun, W.-Y.; Atulasimha, J.; Wang, K. L.; Carman, G. P., Voltage induced artificial ferromagnetic-antiferromagnetic ordering in synthetic multiferroics. *Journal of Applied Physics* **2017,** *122* (22), 224102.

63. Wu, L. Z.; Ding, J.; Jiang, H. B.; Neo, C. P.; Chen, L. F.; Ong, C. K., High frequency complex permeability of iron particles in a nonmagnetic matrix. *Journal of Applied Physics* **2006,** *99* (8), 083905.

64. Bregar, V. B., Advantages of ferromagnetic nanoparticle composites in microwave absorbers. *IEEE Transactions on Magnetics* **2004,** *40* (3), 1679-1684.

65. Buznikov, N. A.; Iakubov, I. T.; Rakhmanov, A. L.; Sboychakov, A. O., High-frequency magnetic permeability of nanocomposite film. *Journal of Magnetism and Magnetic Materials* **2005,** *293* (3), 938-946.

66. Lu, B.; Dong, X. L.; Huang, H.; Zhang, X. F.; Zhu, X. G.; Lei, J. P.; Sun, J. P., Microwave absorption properties of the core/shell-type iron and nickel nanoparticles. *Journal of Magnetism and Magnetic Materials* **2008,** *320* (6), 1106-1111.

67. Zhang, X. F.; Dong, X. L.; Huang, H.; Liu, Y. Y.; Wang, W. N.; Zhu, X. G.; Lv, B.; Lei, J. P.; Lee, C. G., Microwave absorption properties of the carbon-coated nickel nanocapsules. *Applied Physics Letters* **2006,** *89* (5), 053115.

68. Park, J. H.; Shin, H. H.; Jang, H. M., Quasi-intrinsic magnetoelectric coupling in multiferroic nanocomposite thin films. *Physical Review B* **2008,** *77* (21), 212409.

69. Liu, M.; Li, X.; Lou, J.; Zheng, S.; Du, K.; Sun, N. X., A modified sol-gel process for multiferroic nanocomposite films. *Journal of Applied Physics* **2007,** *102* (8), 083911.

70. Wan, J.-g.; Zhang, H.; Wang, X.; Pan, D.; Liu, J.-m.; Wang, G., Magnetoelectric CoFe2O4-lead zirconate titanate thick films prepared by a polyvinylpyrrolidone-assisted sol-gel method. *Applied Physics Letters* **2006,** *89* (12), 122914.

71. Ryu, H.; Murugavel, P.; Lee, J. H.; Chae, S. C.; Noh, T. W.; Oh, Y. S.; Kim, H. J.; Kim, K. H.; Jang, J. H.; Kim, M.; Bae, C.; Park, J. G., Magnetoelectric effects of nanoparticulate Pb(Zr0.52Ti0.48)O3–NiFe2O4 composite films. *Applied Physics Letters* **2006,** *89* (10), 102907.

72. Wan, J. G.; Wang, X. W.; Wu, Y. J.; Zeng, M.; Wang, Y.; Jiang, H.; Zhou, W. Q.; Wang, G. H.; Liu, J. M., Magnetoelectric CoFe2O4–Pb(Zr,Ti)O3 composite thin films derived by a sol-gel process. *Applied Physics Letters* **2005,** *86* (12), 122501.

73. Zhong, X. L.; Wang, J. B.; Liao, M.; Huang, G. J.; Xie, S. H.; Zhou, Y. C.; Qiao, Y.; He, J. P., Multiferroic nanoparticulate Bi3.15Nd0.85Ti3O12–CoFe2O4 composite thin films prepared by a chemical solution deposition technique. *Applied Physics Letters* **2007,** *90* (15), 152903.

74. Chen, W.; Wang, Z. H.; Zhu, W.; Tan, O. K., Ferromagnetic, ferroelectric and dielectric properties of Pb(Zr 0.53 Ti 0.47)O 3 /CoFe 2 O 4 multiferroic composite thick films. *Journal of Physics D: Applied Physics* **2009,** *42* (7), 075421.

75. Chen, W.; Wang, Z.; Ke, C.; Zhu, W.; Tan, O., Preparation and characterization of Pb (Zr0. 53Ti0. 47) O3/CoFe2O4 composite thick films by hybrid sol–gel processing. *Materials Science and Engineering: B* **2009,** *162* (1), 47-52.

76. McDannald, A.; Staruch, M.; Sreenivasulu, G.; Cantoni, C.; Srinivasan, G.; Jain, M., Magnetoelectric coupling in solution derived 3-0 type PbZr0.52Ti0.48O3:xCoFe2O4 nanocomposite films. *Applied Physics Letters* **2013,** *102* (12), 122905.

77. McDannald, A.; Ye, L.; Cantoni, C.; Gollapudi, S.; Srinivasan, G.; Huey, B. D.; Jain, M., Switchable 3-0 magnetoelectric nanocomposite thin film with high coupling. *Nanoscale* **2017,** *9* (9), 3246-3251.

78. Bai, W.; Meng, X.; Lin, T.; Zhu, X.; Tian, L.; Sun, J.; Chu, J., Magnetic Field Induced Dielectric and Ferroelectric Behaviors in Pb(Zr0.5Ti0.5)O3/CoFe2O4 0-3 Thick Composite Films. *Ferroelectrics* **2010,** *410* (1), 50-58.

79. Kim, H. K. D.; Schelhas, L. T.; Keller, S.; Hockel, J. L.; Tolbert, S. H.; Carman, G. P., Magnetoelectric Control of Superparamagnetism. *Nano Letters* **2013,** *13* (3), 884-888.

80. Buzzi, M.; Chopdekar, R. V.; Hockel, J. L.; Bur, A.; Wu, T.; Pilet, N.; Warnicke, P.; Carman, G. P.; Heyderman, L. J.; Nolting, F., Single Domain Spin Manipulation by Electric Fields in Strain Coupled Artificial Multiferroic Nanostructures. *Physical Review Letters* **2013,** *111* (2), 027204.

81. Wu, T.; Bur, A.; Wong, K.; Leon Hockel, J.; Hsu, C.-J.; Kim, H. K.; Wang, K. L.; Carman, G. P., Electric-poling-induced magnetic anisotropy and electric-field-induced magnetization reorientation in magnetoelectric Ni/(011)[Pb (Mg1/3Nb2/3) O3](1-x)-[PbTiO3] x heterostructure. *Journal of applied physics* **2011,** *109* (7), 07D732.

82. Wu, T.; Bur, A.; Wong, K.; Zhao, P.; Lynch, C. S.; Amiri, P. K.; Wang, K. L.; Carman, G. P., Electrical control of reversible and permanent magnetization reorientation for magnetoelectric memory devices. *Applied Physics Letters* **2011,** *98* (26), 262504.

83. de Julián Fernández, C., Influence of the temperature dependence of anisotropy on the magnetic behavior of nanoparticles. *Physical Review B* **2005,** *72* (5), 054438.

84. Li, F.; Zhang, S.; Xu, Z.; Wei, X.; Luo, J.; Shrout, T. R., Piezoelectric activity of relaxor-PbTiO 3 based single crystals and polycrystalline ceramics at cryogenic temperatures: Intrinsic and extrinsic contributions. *Applied physics letters* **2010,** *96* (19), 192903.

85. Eerenstein, W.; Wiora, M.; Prieto, J.; Scott, J.; Mathur, N., Giant sharp and persistent converse magnetoelectric effects in multiferroic epitaxial heterostructures. *Nature materials* **2007,** *6* (5), 348.

86. Brintlinger, T.; Lim, S.-H.; Baloch, K. H.; Alexander, P.; Qi, Y.; Barry, J.; Melngailis, J.; Salamanca-Riba, L.; Takeuchi, I.; Cumings, J., In situ observation of reversible nanomagnetic switching induced by electric fields. *Nano letters* **2010,** *10* (4), 1219-1223.

87. Geprägs, S.; Brandlmaier, A.; Opel, M.; Gross, R.; Goennenwein, S., Electric field controlled manipulation of the magnetization in Ni/BaTiO 3 hybrid structures. *Applied Physics Letters* **2010,** *96* (14), 142509.

88. Streubel, R.; Köhler, D.; Schäfer, R.; Eng, L. M., Strain-mediated elastic coupling in magnetoelectric nickel/barium-titanate heterostructures. *Physical Review B* **2013,** *87* (5), 054410.

89. Chopdekar, R.; Suzuki, Y., Magnetoelectric coupling in epitaxial Co Fe 2 O 4 on Ba Ti O 3. *Applied physics letters* **2006,** *89* (18), 182506.

90. Zavaliche, F.; Zhao, T.; Zheng, H.; Straub, F.; Cruz, M.; Yang, P.-L.; Hao, D.; Ramesh, R., Electrically assisted magnetic recording in multiferroic nanostructures. *Nano letters* **2007,** *7* (6), 1586-1590.

91. Zhang, S.; Zhao, Y.; Xiao, X.; Wu, Y.; Rizwan, S.; Yang, L.; Li, P.; Wang, J.; Zhu, M.; Zhang, H., Giant electrical modulation of magnetization in Co 40 Fe 40 B 20/Pb (Mg 1/3 Nb 2/3) 0.7 Ti 0.3 O 3 (011) heterostructure. *Scientific reports* **2014,** *4*, 3727.

92. Liu, M.; Zhou, Z.; Nan, T.; Howe, B. M.; Brown, G. J.; Sun, N. X., Voltage Tuning of Ferromagnetic Resonance with Bistable Magnetization Switching in Energy-Efficient Magnetoelectric Composites. *Advanced Materials* **2013,** *25* (10), 1435-1439.

93. Zhang, S.; Zhao, Y.; Li, P.; Yang, J.; Rizwan, S.; Zhang, J.; Seidel, J.; Qu, T.; Yang, Y.; Luo, Z., Electric-field control of nonvolatile magnetization in Co 40 Fe 40 B 20/Pb (Mg 1/3 Nb 2/3) 0.7 Ti 0.3 O 3 structure at room temperature. *Physical review letters* **2012,** *108* (13), 137203.

94. Sergienko, I. A.; Dagotto, E., Role of the Dzyaloshinskii-Moriya interaction in multiferroic perovskites. *Physical Review B* **2006,** *73* (9), 094434.

95. Yamasaki, Y.; Miyasaka, S.; Kaneko, Y.; He, J.-P.; Arima, T.; Tokura, Y., Magnetic reversal of the ferroelectric polarization in a multiferroic spinel oxide. *Physical review letters* **2006,** *96* (20), 207204.

96. Mair, L. O.; Martinez-Miranda, L. J.; Kurihara, L. K.; Nacev, A.; Hilaman, R.; Chowdhury, S.; Jafari, S.; Ijanaten, S.; da Silva, C.; Baker-McKee, J., Electric-field responsive contrast agent based on liquid crystals and magnetic nanoparticles. *AIP Advances* **2018,** *8* (5), 056731.

97. Ryu, H.; Murugavel, P.; Lee, J.; Chae, S.; Noh, T.; Oh, Y. S.; Kim, H. J.; Kim, K. H.; Jang, J. H.; Kim, M., Magnetoelectric effects of nanoparticulate Pb (Zr 0.52 Ti 0.48) O 3–Ni Fe 2 O 4 composite films. *Applied Physics Letters* **2006,** *89* (10), 102907.

98. Wan, J.; Wang, X.; Wu, Y.; Zeng, M.; Wang, Y.; Jiang, H.; Zhou, W.; Wang, G.; Liu, J.-M., Magnetoelectric CoFe 2 O 4–Pb (Zr, Ti) O 3 composite thin films derived by a sol-gel process. *Applied Physics Letters* **2005,** *86* (12), 122501.

99. Zhong, X.; Wang, J.; Liao, M.; Huang, G.; Xie, S.; Zhou, Y.; Qiao, Y.; He, J., Multiferroic nanoparticulate Bi 3.15 Nd 0.85 Ti 3 O 12–Co Fe 2 O 4 composite thin films prepared by a chemical solution deposition technique. *Applied physics letters* **2007,** *90* (15), 152903.

100. Zhang, J.; Dai, J.; So, L.; Sun, C.; Lo, C.; Or, S.; Chan, H. L., The effect of magnetic nanoparticles on the morphology, ferroelectric, and magnetoelectric behaviors of CFO/P (VDF-TrFE) 0–3 nanocomposites. *Journal of Applied Physics* **2009,** *105* (5), 054102.

101. Kobayashi, K.; Horiuchi, S.; Kumai, R.; Kagawa, F.; Murakami, Y.; Tokura, Y., Electronic ferroelectricity in a molecular crystal with large polarization directing antiparallel to ionic displacement. *Physical review letters* **2012,** *108* (23), 237601.

102. Horiuchi, S.; Tokura, Y., Organic ferroelectrics. *Nature materials* **2008,** *7* (5), 357.

103. Lemée-Cailleau, M.; Le Cointe, M.; Cailleau, H.; Luty, T.; Moussa, F.; Roos, J.; Brinkmann, D.; Toudic, B.; Ayache, C.; Karl, N., Thermodynamics of the neutral-to-ionic transition as condensation and crystallization of charge-transfer excitations. *Physical review letters* **1997,** *79* (9), 1690.

104. Giallonardo, J.; Erb, U.; Aust, K.; Palumbo, G., The influence of grain size and texture on the Young's modulus of nanocrystalline nickel and nickel–iron alloys. *Philosophical Magazine* **2011,** *91* (36), 4594-4605.

105. Lapidus, S. H.; Naik, A.; Wixtrom, A.; Massa, N. E.; Ta Phuoc, V.; Del Campo, L.; Lebègue, S. b.; Ángyán, J. n. G.; Abdel-Fattah, T.; Pagola, S., The black polymorph of TTF-CA: TTF polymorphism and solvent effects in mechanochemical and vapor digestion syntheses, FT-IR, crystal packing, and electronic structure. *Crystal Growth & Design* **2013,** *14* (1), 91-100.

106. Goya, G.; Fonseca, F.; Jardim, R.; Muccillo, R.; Carreno, N.; Longo, E.; Leite, E., Magnetic dynamics of single-domain Ni nanoparticles. *Journal of applied physics* **2003,** *93* (10), 6531-6533.

107. Kechrakos, D.; Trohidou, K., Magnetic properties of dipolar interacting single-domain particles. *Physical Review B* **1998,** *58* (18), 12169.

108. Fonseca, F.; Goya, G.; Jardim, R.; Muccillo, R.; Carreno, N.; Longo, E.; Leite, E., Superparamagnetism and magnetic properties of Ni nanoparticles embedded in SiO 2. *Physical Review B* **2002,** *66* (10), 104406.

109. Vargas, J.; Nunes, W.; Socolovsky, L.; Knobel, M.; Zanchet, D., Effect of dipolar interaction observed in iron-based nanoparticles. *Physical Review B* **2005,** *72* (18), 184428.

110. Bae, C. J.; Hwang, Y.; Park, J.; An, K.; Lee, Y.; Lee, J.; Hyeon, T.; Park, J.-G., Inter-particle and interfacial interaction of magnetic nanoparticles. *Journal of Magnetism and Magnetic Materials* **2007,** *310* (2), e806-e808.

111. Pauly, M.; Pichon, B. P.; Panissod, P.; Fleutot, S.; Rodriguez, P.; Drillon, M.; Begin-Colin, S., Size dependent dipolar interactions in iron oxide nanoparticle monolayer and multilayer Langmuir–Blodgett films. *Journal of Materials Chemistry* **2012,** *22* (13), 6343-6350.

112. Woińska, M.; Szczytko, J.; Majhofer, A.; Gosk, J.; Dziatkowski, K.; Twardowski, A., Magnetic interactions in an ensemble of cubic nanoparticles: A Monte Carlo study. *Physical Review B* **2013,** *88* (14), 144421.

113. Nadeem, K.; Krenn, H.; Traußnig, T.; Würschum, R.; Szabó, D.; Letofsky-Papst, I., Effect of dipolar and exchange interactions on magnetic blocking of maghemite nanoparticles. *Journal of Magnetism and Magnetic Materials* **2011,** *323* (15), 1998-2004.

114. Poddar, P.; Telem-Shafir, T.; Fried, T.; Markovich, G., Dipolar interactions in two-and three-dimensional magnetic nanoparticle arrays. *Physical Review B* **2002,** *66* (6), 060403.

115. Dormann, J.; Fiorani, D.; Tronc, E., On the models for interparticle interactions in nanoparticle assemblies: comparison with experimental results. *Journal of Magnetism and Magnetic Materials* **1999,** *202* (1), 251-267.

116. Moscoso-Londoño, O.; Tancredi, P.; Muraca, D.; Zélis, P. M.; Coral, D.; van Raap, M. F.; Wolff, U.; Neu, V.; Damm, C.; De Oliveira, C., Different approaches to analyze the dipolar interaction effects on diluted and concentrated granular superparamagnetic systems. *Journal of Magnetism and Magnetic Materials* **2017,** *428*, 105-118.

117. Nunes, W.; Cebollada, F.; Knobel, M.; Zanchet, D., Effects of dipolar interactions on the magnetic properties of γ-Fe 2 O 3 nanoparticles in the blocked state. *Journal of applied physics* **2006,** *99* (8), 08N705.

118. Timopheev, A.; Ryabchenko, S.; Kalita, V.; Lozenko, A.; Trotsenko, P.; Stephanovich, V.; Grishin, A. M.; Munakata, M., The influence of intergranular interaction on the magnetization of the ensemble of oriented Stoner–Wohlfarth nanoparticles. *Journal of Applied Physics* **2009,** *105* (8), 083905.

119. Timopheev, A.; Bdikin, I.; Lozenko, A.; Stognei, O.; Sitnikov, A.; Los, A.; Sobolev, N., Superferromagnetism and coercivity in Co-Al2O3 granular films with perpendicular anisotropy. *Journal of Applied Physics* **2012,** *111* (12), 123915.

120. Toulemon, D.; Rastei, M. V.; Schmool, D.; Garitaonandia, J. S.; Lezama, L.; Cattoën, X.; Bégin-Colin, S.; Pichon, B. P., Enhanced collective magnetic properties induced by the controlled

assembly of iron oxide nanoparticles in chains. *Advanced Functional Materials* **2016,** *26* (15), 2454-2462.